THE ASTROPHYSICAL JOURNAL, 551:1073–1098, 2001 April 20

A SPATIALLY RESOLVED, SEMIEMPIRICAL MODEL FOR THE EXTENDED ATMOSPHERE OF α ORIONIS (M2 IAB)

GRAHAM M. HARPER AND ALEXANDER BROWN
Center for Astrophysics and Space Astronomy, University of Colorado, Boulder, CO 80309-0389: gmh@casa.colorado.edu, ab@casa.colorado.edu
AND
JEREMY LIM
Academia Sinica Institute of Astronomy and Astrophysics, PO Box 1-87, Nankang, Taipei 115, Taiwan, jlim@asiaa.sinica.edu.tw
Received 2000 April 21; accepted 2000 December 19

ABSTRACT

We have constructed a detailed mean density and temperature model for the extended outer atmosphere of the O-rich supergiant Betelgeuse (α Ori [M2 Iab]), which extends from 1.0 to 10.0 stellar radii. A one-dimensional model is based on fitting NRAO[1] VLA centimeter visibility data, and two-dimensional models are constructed using the intensity contours of the 0.7 cm observations of Lim et al. As one moves in toward the star from about 10 R_* the mean electron temperature increases to a value of $\simeq$3800 K, then declines down below $T_{\rm eff}$, and then rises to photospheric values. The peak mean model temperature is less than the typical chromospheric temperatures found in previous models. Observations of Hα and chromospheric ultraviolet (UV) emission show that higher temperature components must also exist, but they do not dominate the weighted mean temperature structure. We tentatively identify the radius where the temperature distribution peaks ($R \simeq 1.45\ R_*$) with the dominant chromospheric UV emission region and find an areal filling factor of $\leq \frac{1}{4}$. In the extended semiempirical model the dominant source of electrons is from photoionized metals and is dominated by carbon. The low ionization of hydrogen leads to a dominance by H^- (free-free) opacity at centimeter wavelengths. We derive simple estimates of the radio spectral indices for other similar M supergiants. We have constructed two-dimensional models to examine whether the intensity asymmetry observed at 0.7 cm is most likely to result from density or temperature variations. Adopting an elliptical two-dimensional model, a density asymmetry along the axes of symmetry would need to be 20:1. If we assume the radial wind velocity is independent of angle the integrated mass-loss rate is only a factor of $\sim$2 greater than that derived from the one-dimensional model. However, previous Hα speckle observations that sample the same spatial regions suggest the asymmetry observed at 0.7 cm is not due to such a large-scale density asymmetry. A modest change in temperature can more easily provide the asymmetry, increasing both the opacity and the thermal source term. If the radial density structure is assumed to be the same as in 1992 September, when *HST*/GHRS spectra were obtained, then the Fe II wind absorption features provide an estimate of the mass-loss rate of $3.1(\pm 1.3) \times 10^{-6}\ M_\odot\ {\rm yr}^{-1}$. This further implies that the cool material dominates the mass of the extended atmosphere and that the radio-emitting region is within the base of the outflow observed in the circumstellar layers. A simple silicate dust model is constructed and the semiempirical model suggests an onset of dust formation at $R \simeq 33\ R_*$ where $T_{\rm dust} \sim 360$ K. This region lies outside the semiempirical model but simple extrapolations suggest that at this radius $T_e \sim 220$ K, and the mean hydrogen density $n_{\rm H} \sim 3 \times 10^6\ {\rm cm}^{-3}$. We address the difficult question of whether the mean thermal model based on the radio data can be consistent with the observed off-limb Hα scattering emission if inhomogeneities are present.

Subject headings: circumstellar matter — stars: atmospheres — stars: chromospheres — stars: mass loss — supergiants

1. INTRODUCTION

The outer atmosphere of the O-rich (O/C = 2.5; Lambert et al. 1984) supergiant Betelgeuse (α Ori [M2 Iab]) has been the subject of intensive study. Its large angular size and brightness makes it an ideal subject of multiwavelength studies. The mass-loss rate ($\sim 4 \times 10^{-6}\ M_\odot\ {\rm yr}^{-1}$; Glassgold & Huggins 1986) is sufficiently large so that the extended envelope has also been imaged. Betelgeuse is, therefore, a prime target for studies of the still unknown mechanisms that lead to mass loss. Until recently the physical conditions within the first 10 stellar radii (10 R_*) were generally assumed to consist of a warm, extended region with electron temperatures near 8000 K, where partially ionized hydrogen dominates the electron density (Wischnewski & Wendker 1981; Newell & Hjellming 1982; Hartmann & Avrett 1984; Skinner et al. 1997). However, Very Large Array (VLA) radio observations, obtained at five wavelengths, resolved α Ori and showed that the mean electron temperature is much cooler, i.e., T_e = 2000–4000K (Lim et al. 1998). The aim of this paper is to construct a physical model that reproduces the radio observations and provides estimates of electron temperature and hydrogen and electron densities ($n_{\rm H}$, n_e) as a function of radius.

Table 1 gives a partial compilation of observations that indicate the extended nature of α Ori's atmosphere and wind, and includes estimates of the characteristic wind crossing time (assuming $V_{\rm wind} \sim 10$ km s^{-1} for simplicity).

[1] The National Radio Astronomy Observatory is a facility of the national Science Foundation operated under cooperative agreement by Associated Universities, Inc.

TABLE 1

A PARTIAL COMPILATION OF OBSERVATIONS OF THE EXTENDED ENVELOPE OF α ORI

Radial Extent (arcsec)	Diagnostic	Wind Crossing-Time (yr)	Reference
420	*IRAS* 60 μm	26,000	Noriega-Crespo et al. 1999
90	polarized B	5600	McMillan & Tapia (1978)
90	polarized UBV	5600	Le Borgne et al. (1986)
50	K I λ7699 Å	3100	Honeycutt et al. (1980)
17	Na I λ5896 Å	1000	Mauron (1990)
8	K I λ7699 Å	500	Bernat & Lambert (1975)
4	8.2μm, 9.7 μm	250	Skinner et al. (1997)
0.16	6 cm	...	Lim et al. (1998)
0.14	GHRS Mg II h & k	...	Uitenbroek et al (1998)
0.13	11.15 μm	...	Bester et al. (1996)
0.13	Hα	...	Hebden et al. (1987)
0.06	FOC UV continuum	...	Gilliland & Dupree (1996)

The circumstellar envelope has been studied in the K I resonance lines by Bernat & Lambert (1975, 1976), Honeycutt et al. (1980), and Mauron & Caux (1992). Mauron (1990) also studied α Ori in the Na I λ5896 line. The circumstellar envelope of Betelgeuse has recently been imaged at 10 μm using a nulling interferometer (Hinz et al. 1998), and imaged at 11.7 and 17.9 μm by Rinehart, Hayward, & Houck (1998). These studies confirm dust nebulosity out to $\sim 5''$. The dust shell surrounding α Ori is optically thin at 9.7 μm ($\tau_{9.7\ \mu m} = 0.06$; Skinner & Whitmore 1987). On the largest scales, α Ori was detected as an extended *IRAS* source at 60 μm (Stencel, Pesce, & Hagen Bauer 1988). Noriega-Crespo et al. (1997) reported enhanced resolution *Infrared Astronomical Satellite* (*IRAS*) 60 and 100 μm images that may show a parsec-size bow shock at $\sim 7'$. These observations mostly relate to the outer reaches of the stellar wind. The physical conditions in these circumstellar layers have been the subject of detailed study: The ionization and temperature structure have been studied by Glassgold & Huggins (1986) and Rodgers & Glassgold (1991), respectively. New constraints on the circumstellar environment have been obtained with *Infrared Space Observatory* (*ISO*) (Justtanont et al. 1999; Barlow 1999).

Closer to the stellar surface, Lambert & Snell (1975) have examined the chromospheric contribution to the observed IR spectrum, and semiempirical chromospheric models of α Ori were constructed from spatially unresolved optical and ultraviolet *International Ultraviolet Explorer* (*IUE*) spectra by Basri, Linsky, & Eriksson (1981). More recently, the chromosphere has been partially spatially resolved with the *Hubble Space Telescope* (Gilliland & Dupree 1996; Uitenbroek, Dupree, & Gilliland 1998), with the star in the ultraviolet appearing to be about twice the size of the optical photosphere in the continuum and even more extended in the Mg II *H* and *K* lines. Given the findings described in this paper, we eagerly await quantitative models derived from these UV images and spectra. Ground-based observations have been made that sample the inner 5 R_*, including Hα speckle interferometry (Hebden et al. 1986) and diffraction limited speckle images (Hebden, Eckhart, & Hege 1987; Christou, Hebden, & Hege 1988). Models have yet to be constructed that examine the physical conditions within the Hα scattering region.

Typically the terminal wind velocity of evolved late-type stellar winds is less than the surface escape speed (Holzer & MacGregor 1985). An important region for studying the wind acceleration is, therefore, the first few stellar radii where most of the energy and momentum are deposited within the flow. Few stars have large enough angular scales to provide direct information on this region. Most information on this region has come from the ζ Aurigae eclipsing binary systems (see review by Dupree & Reimers 1987), but in many systems this is where the stellar winds and orbital motions have comparable velocities and the binarity is likely to affect the flows making analysis problematic, e.g., Walder & Harper (1996). Betelgeuse's angular size makes it ideal for the study of extended atmospheres of single stars, with the further benefit that the indirect role of dust on the mass flow can also be assessed, as the dust shells have been imaged. The VLA observations of Skinner et al. (1996, 1997) and Lim et al. (1998) allow spatial information on the temperature and density to be inferred for the region within 10 R_*. The radio spectrum of α Ori has a similar spectral index to α Sco (M1 1ab) (Hjellming & Newell 1983), and it is our hope that insight gleaned from α Ori may help in the understanding of other M supergiants.

Skinner et al. (1997) constructed semiempirical models based on infrared (IR) and radio data. These models seem to indicate the presence of a warm extended chromosphere suggested both by previous radio models, and the theoretical constant damping length, Alfvén wave-driven wind model of Hartmann & Avrett (1984). However, Lim et al. (1998) presented VLA radio visibility data that resolved the atmosphere of α Ori in five bands from 0.7 to 6 cm. These data provide strong empirical evidence that the outer atmosphere is in fact mostly cool and extended, with temperatures a factor of 2–4 smaller than in previous models. Here we seek to construct a physical model constrained by the radio data, which can then be used to examine how the new VLA data can be reconciled with previous ideas and models.

Betelgeuse shows a rich variety of variability, including photospheric radial velocity, photometric (Goldberg 1984 and references therein) and surface structure variations (Tuthill, Haniff, & Baldwin 1997), symmetry changes in chromospheric emission-line profiles, and dust shell variations (Bester et al. 1996). Since these forms of variability are a common feature of semiregular variables, they need to be studied in tandem with the mean extended models described here. The outer dust shell (Sudol et al. 1999, 2000) and wind absorption features, however, do appear to be more stable (Goldberg 1979).

In this paper we focus on the centimeter radio continuum emission, which mostly arises from free-free processes associated with neutral and ionized hydrogen. Radio continuum emission is a powerful diagnostic. The thermal source function is in the Rayleigh-Jeans limit of the Planck function, and therefore almost linear with the electron temperature. This means that, if the atmosphere and wind are inhomogeneous on the small scale, the source function is an average of temperatures in the different components, unlike the ultraviolet (UV), where very small amounts of hot plasma can dominate the total emission, e.g., Carlsson & Stein (1995). Hydrogen is an excellent tracer of matter, and opacity cross sections are known at the percent level. Radio continuum emission is also relatively insensitive to the complex velocity fields, which have profound effects on the analysis of optical and UV line profiles.

We are mindful, however, of the potential role of dust emission, and for completeness and later studies we include a simple dust scattering and absorption model in the radiative transfer computation. Dust can have important effects on the IR spectrum, but inherent uncertainties are present that limit the reliability of dust modeling, above and beyond those associated with the present atmospheric model. These uncertainties include the composition of grains, crystalline structure and surface effects, growth and formation, the shapes, and the size distribution and alignment. We note that potential improvements in dust models may result from studying the variations in narrowband (0.01 μm) visibility curves across dust absorption features (Lorenz-Martins, Lefèvre, & Mékarnia 1995).

In § 2 we discuss the radio and IR data that we will use in the modeling process. We discuss the stellar parameters in § 3, and the radio opacity sources in § 4. In § 5 we describe the modeling procedure, and the semiempirical model (hereafter the SEM) is described in § 6 with the controlling physics being outlined in § 7. The discussion and conclusions are presented in §§ 8 and 9, respectively.

2. RADIO DATA

In Figure 1 we show a compilation of radio and IR fluxes, which are also given in Table 2. The primary data set used to construct the semiempirical model are the radio visibilities from Lim et al. (1998). These data at 0.69, 1.33, 2.01, 3.54, and 6.17 cm span an order of magnitude in wavelength and 2 orders of magnitude in opacity. This range of opacity gives us information on different spatial scales. Although we are primarily concerned with modeling the centimeter-radio observations in the extended atmosphere, we have run the models both down to the stellar surface and out into the circumstellar region in a somewhat less constrained manner, using a previous 20 cm flux and shorter wavelength data ($10 < \mu m < 1000$). Newell & Hjellming (1982) studied radio flux measurements of α Ori and found that most data were consistent with a "normal" spectrum, with two fluxes being a factor of 2 lower and two very high values. We use the normal fluxes to supplement the Lim et al. (1998) data. At 11.15 μm the Infrared Spatial Interferometer (ISI) data of Bester et al. (1996) have spatially resolved the stellar and dust components. This data set allows us to model both the upper photosphere and circumstellar dust region.

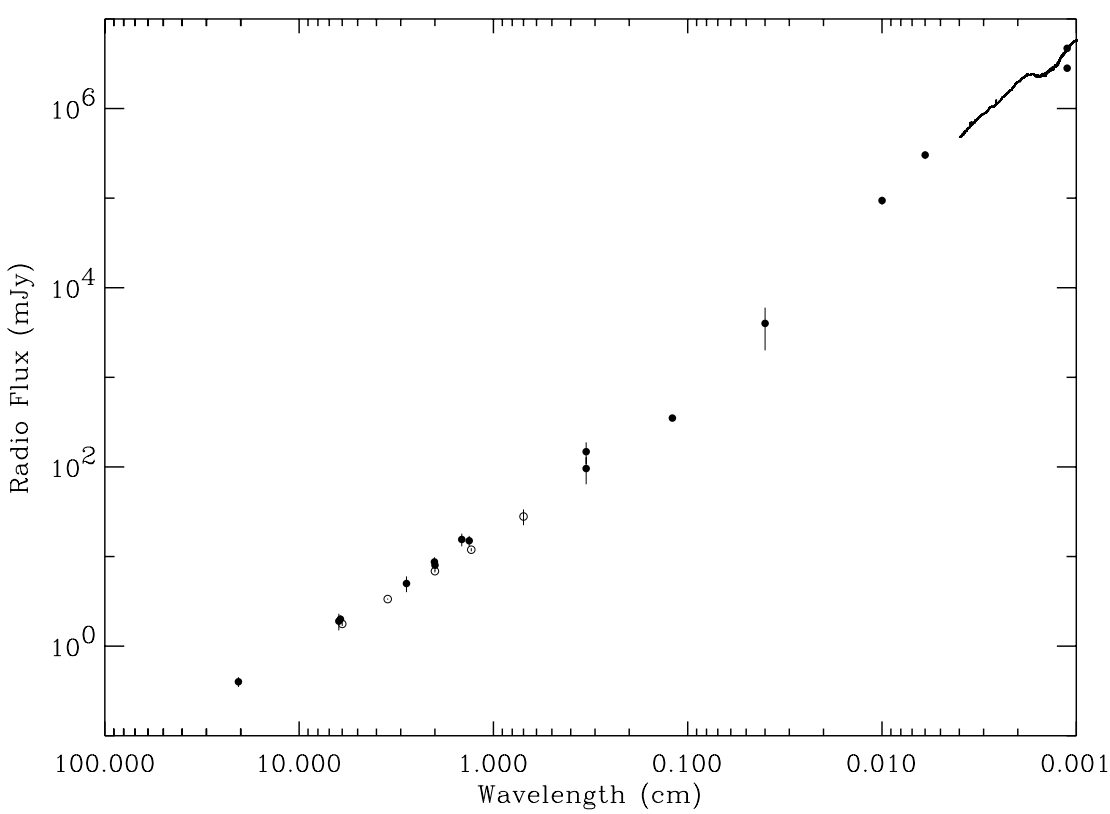

FIG. 1.—Compilation of radio and mid-IR fluxes (*solid circles*), which are used to constrain the semiempirical density and temperature model. Hollow circles indicate the visibility data of Lim et al. (1998). At 11.15 μm we have plotted the flux from the star (*lower*) and the star plus dust (*upper*). The *ISO* spectrum is also shown. These data and error bars give an indication of the time variation and observational uncertainties.

TABLE 2

COMPILATION OF RADIO AND IR FLUXES

Frequency (GHz)	Wavelength	Flux (mJy)	Uncertainty[a] (mJy)	Reference
1.46	20.5 cm	0.4	0.05	1
4.86	6.17 cm	1.77	0.09	2
8.46	3.54 cm	3.35	0.05	2
14.94	2.01 cm	6.86	0.21	2
22.46	1.32 cm	11.92	0.48 (3.0)	2, 3
43.34	6.9 mm	27.96	5.60	2
90.00	3 mm	96–148	40	1
250.0	1.2 mm	351	25	3
	400 μm	4.0×10^3	2.0×10^3	4
	100 μm	9.4×10^4	...	5
	60 μm	3.03×10^5	...	5
	25 μm	1.74×10^6	...	6
	11.15 μm[b]	2.82×10^6	(1.7×10^5)	7
	11.15 μm[c]	1.88×10^6	(1.5×10^5)	7
	$\sum$ 11.15 μm	4.70×10^6	(3.3×10^5)	7
	11.5 μm (total)	4.49×10^6	2.7×10^5	8

[a] In this column we give measurement uncertainties; if the value is in parentheses it indicates the half-range in observed variability.

[b] Stellar contribution.

[c] Dust contribution.

REFERENCES—(1) Newell & Hjellming 1982 normal state; (2) Lim et al. 1998 ; (3) Altenhoff et al. 1994; (4) Sopka et al. 1985; (5) Skinner & Whitmore 1987; (6) Rowan-Robinson et al. 1986; (7) Bester et al. 1996; (8) Sudol et al. 1999.

We have not included the James Clerk Maxwell Telescope (JCMT) 0.7 and 1.1 mm observations of Marshall, Leahy, & Kwok (1992); as discussed by Altenhoff, Thum, & Wendker (1994), these observations have low signal-to-noise (S/N) and seem to be unphysically small.

2.1. *Variability of Centimeter-Radio Fluxes*

α Ori is known to undergo photospheric radial velocity and brightness variations (Smith, Patten, & Goldberg 1989; Goldberg 1984; Dupree et al. 1987). The chromosphere (or ultraviolet line-forming region) may possibly move with the photospheric motions (Boesgaard 1979), while the velocity of wind absorption features appear to be quite steady (Goldberg 1979). Between the photosphere, which moves in and out with an amplitude of ~ 3 km s^{-1}, and the steady wind flow, there lies a region where the mass flow decouples from the photosphere. The radio data may be sampling this dynamic region.

The 6 cm VLA and MERLIN[2] visibility data of Skinner et al. (1997) were obtained on 1990 April 28 and 1992 December 4, respectively, while the multiwavelength VLA data of (Lim et al. 1998) were obtained in 1996 December 21. The 6 cm VLA data sets are in good agreement, while in the MERLIN data α Ori is mostly resolved out. Another clue to the stability of the globally averaged radio-emitting region is provided by the monitoring study of Drake et al. (1992), who monitored α Ori about once a month from 1986 July to 1990 September. They found low-level variability ($\leq 25\%$) at 2.0 and 3.6 cm, and possibly at 6 cm. The variations occurred on timescales as short as 1 month and no correlation was found between wavelengths. The fluxes are also similar to those given by Newell & Hjellming (1982); thus the centimeter-radio fluxes of α Ori appear to be fairly stable. Early single-dish accounts of "flares" are now generally discounted as spurious artifacts, as they have not been detected with radio interferometric arrays where source confusion, calibration problems, and interference are much less of a problem.

Infraed spatial interferometer (ISI) data from Bester et al. (1996) show a possible episode of dust formation near 5 R_* in 1993–1994 as compared to 1988–1992. Our models suggest the 6 cm flux is formed mostly inside this radius (see § 6). In our model we place most weight on the VLA visibility data, and use the flux data to increase the spatial extent and potential usefulness of the model.

3. STELLAR PARAMETERS

Although our model for the extended atmosphere does not require a detailed model for the photosphere it is highly desirable to relate the extended atmospheric model as closely as possible to the photospheric layers. The literature contains a wide range of angular diameter (ϕ_*) and effective temperature ($T_{\rm eff}$) estimates for α Ori (e.g., White 1980; Cheng et al. 1986; Vieira 1986, and references therein). There are several sources of uncertainty in the ϕ_* and $T_{\rm eff}$ estimates; intrinsic temporal and structural variability, interstellar medium (ISM) reddening correction for the bolometric flux, and limb-darkening correction for the multiwavelength angular diameter observations.

The *Hipparcos* parallax (ESA 1997) gives a distance of 131^{+36}_{-23} pc, which is closer than many previous estimates. Given this smaller distance, there is little reason to expect significant ISM reddening in the line of sight toward α Ori. Estimates of interstellar hydrogen column density[3] and reddening are $N_{\rm H\,I} \sim 3 \times 10^{19}$ cm^{-2} and $E(B-V) < 0.1$ (Paresce 1984). More recent models of the local ISM suggest $2 \times 10^{18} < N_{\rm H\,I}({\rm cm}^{-2}) < 1 \times 10^{20}$ (J. L. Linsky, 2000, private communication). Adopting a mean reddening conversion of $N_{\rm H\,I} = 5.5 \times 10^{21}\ E(B-V)$ (Black 1987), which is probably not meaningful for these low columns, and a likely upper estimate of $N_{\rm H\,I} = 1 \times 10^{20}$ cm^{-2}, we find $E(B-V) \leq 0.02$, or $A_V \leq 0.06$. In this paper we correct for this small reddening using the ISM reddening model of Cardelli, Clayton, & Mathis (1989) with $R_V = A_V/E(B-V) = 3.09$.

ϕ^1 Ori has an angular separation of 5°.5 from α Ori and lies at ~ 300 pc; ϕ^1 Ori has an estimated $E(B-V) = 0.11$ (Fruscione et al. 1994), suggesting that in this general direction there is little ISM material to redden the α Ori spectrum. On arcminute scales there is structure in the ISM toward α Ori (Knapp & Bowers 1988); however, since the flux peak of α Ori is near 1–2 μm, the presence of additional ISM material would imply only a small correction would be needed to the bolometric flux. Circumstellar reddening from dust is not expected to be significant in the red and near-IR, and in any case, the bolometric flux ($F_{\rm Bol}$) can be recovered by including the IR dust emission, which is repro-

[2] MERLIN: the Multi-Element Radio Linked Interferometer Network, a national facility operated by the University of Manchester on behalf of PPARC

[3] Throughout this paper we adopt the following standard convention: particle densities are denoted by lowercase n, e.g., $n_{\rm H}$ (cm^{-3}), while column densities are denoted with the uppercase N, e.g., $N_{\rm H}$ (cm^{-2})

cessed photospheric emission. Establishing $F_{\rm bol}$ empirically is problematic but not such a severe problem as for the angular diameter (see below). Observations do not exist that adequately sample the stellar flux distribution at different times to measure meaningful temporal variations of $F_{\rm Bol}$. Proxies, such as those described below, provide indirect means of estimating $F_{\rm Bol}$. The V magnitude of α Ori varies from 0.4 to 0.8 and is sensitive to $T_{\rm eff}$ through the strength of the TiO absorption bands.

We have estimated the flux distribution for α Ori by combining several spectral segments; *HST*/Goddard High Resolution Spectrograph 1200–3300 Å (Carpenter et al. 1994b; Carpenter & Robinson 1997); spectrophotometry 3600–8700 Å (Kiehling 1987); scaled synthetic spectrum for evolved M stars 8700 Å 1.43 μm (B. Plez, 1997, private communication); spectral segment from AZ Cyg (M2 Ia) 1.43–2.5 μm (Lançcon & Rocca-Volmerange 1992); *ISO* Short Wavelength Spectrometer 2.36–44.0 μm (Justtanont et al. 1999); *IRAS* 60 and 100 μm. The Kiehling (1987) spectrophotometry corresponds to $V = 0.40$, while the *ISO* data were obtained when α Ori was visually fainter, as judged by the photometry of Morgan, Wasatonic, & Guinan (1997). For reference, Table 3 gives the Johnson-Cousins *UBVRI* and Johnson-Glass *JHKL* colors computed from the adopted flux distribution using the passbands defined by Bessell (1990) and Bessell & Brett (1988), respectively, and the zero-point magnitudes given by Bessell, Castelli, & Plez (1998).

We estimate $F_{\rm bol} = 1.02 \pm 0.06 \times 10^{-4}$ ergs cm $^{-2}$ s^{-1} after the small ISM correction. The given uncertainty is a crude estimate based on trial interpolations between the Kiehling (1987), the *ISO* and scaled Lançon & Rocca-Volmerange (1992) spectral segments, and is not intended as a rigorous estimate. There is an additional systematic uncertainty from the absolute flux calibration. The dominant uncertainty in $F_{\rm Bol}$ lies with our poor knowledge of the absolute flux distribution near the flux peak. This flux distribution corresponds to an epoch when α Ori was bright in the V band ($V = 0.40$), and we may expect this to be close to the upper limit of $F_{\rm Bol}$. Dyck et al. (1992, 1996) estimated an dereddened value of $F_{\rm bol} = 1.08$–1.15×10^{-4} ergs cm^{-2} s^{-1}, with $A_V \simeq 0.46$.

The apparent angular size of Betelgeuse is a strong function of wavelength, and from a modeling standpoint it is desirable to choose an angular diameter that can reasonably be related to known physical conditions in the photosphere. The high opacities in line cores and molecular bands leads these wavelengths to be unsuitable choices, continuum wavelengths are more suitable.

$T_{\rm eff}$ can be estimated by

$$T_{\rm eff} \simeq 2.341 \times 10^5 \left(\frac{F_{\rm Bol}}{\phi_{\rm Ros}^2}\right)^{0.25} \ {\rm K}\ , \qquad (1)$$

where $\phi_{\rm Ros}$ is the angular diameter in milliarcsec (mas) corresponding to a Rosseland optical depth $\tau_{\rm Ros} = \frac{2}{3}$. For a discussion on the choice of suitable reference stellar radii for extended stellar atmospheres see Baschek, Scholz, & Wehrse (1991). Previous published values of $T_{\rm eff}$ based on bolometric fluxes that included significant dereddening, as high as $A_V = 0.7$, have overestimated $T_{\rm eff}$. Note that the (Tsuji 1978) value of $T_{\rm eff} = 3900$K has now been revised downward, using the Infrared Flux Method (Blackwell & Shallis 1977) to 3600 ± 150K (Tsuji et al. 1994).

Deriving $\phi_{\rm Ros}$ from multiwavelength, uniform-disk angular diameter measurements ($\phi_{\rm UD}$) is potentially complicated by several factors. These include the presence of a dust-scattering halo (Tsuji 1978), the presence of discrete structures emitting ~10% flux on the stellar disk (Tuthill et al. 1997), and the need for detailed model limb-darkening corrections (Scholz & Takeda 1987; Hofmann & Scholz 1998). Measurements of the wavelength dependent $\phi_{\rm UD}$ have considerable scatter, ranging from $38 < \phi_{\rm UD}({\rm mas}) < 69$, which have yet to be modeled satisfactorily (see Fig 3 of White 1980 and Fig. 2 of Tsuji 1978). Wilson, Dhillon, & Haniff (1997) report the presence of a dust halo and make an allowance for the dust in their $\phi_{\rm UD}$ determination. The presence of an asymmetric photospheric intensity distribution at some epochs seems to be firmly established (Klückers et al. 1997; Burns et al. 1997). These asymmetries may affect some previous angular diameter measurements, although these "hot spots" are not always present. Different values of $\phi_{\rm UD}$ are derived when the presence of spots is included or ignored in the analysis, for example , in Tuthill et al. 1997, who find that $\phi_{\rm UD}$ is typically more than 10% larger when a disk plus hot-spot model is employed.

Morgan et al. (1997) have monitored α Ori with V-band and Wing three-filter observations. The selected bands provide measures for the near infrared magnitude (1.024 μm), IR color, and effective temperature (from the TiO absorption bands). Morgan et al. find that the systematic changes in effective temperature correspond to changes in luminosity, while the inferred radius does not change significantly. Bester et al. (1996) also find that most of the changes in visible magnitude result from changes in temperature rather than size. These results argue against significant global changes in size, which means we need to consider other alternatives to explain the wide scatter of ϕ found in the literature. Given the variable nature of α Ori and the current uncertainty in the interpretation of the angular diameter observations, we shall adopt a ϕ_* and later discuss the effects on the semiempirical model if we had adopted different values.

3.1. *Adopted Fudicial Inner Radius*

An angular scale and reference radius are required to derive the spatial scale of the semiempirical radio model. We use the estimate of $F_{\rm bol} = 1.02 \times 10^{-4}$ ergs cm^{-2} s^{-1} and an angular diameter of 56 mas from the 11.15 μm ISI visibility data of Bester et al. (1996) to define a fudicial radius and an estimate of $T_{\rm eff}$. The reference angular diameter determined at 11.15 μm (Bester et al. 1996) is expected to be less sensitive to temperature inhomogeneities than optical values as the source function lies on the Rayleigh-Jeans tail. Hereafter, we refer to the fudicial radius as R_*. We note that most previous atmospheric models of α Ori adopted a larger distance and therefore direct comparison of our results to previous work requires some care. Specifically, we adopt $\phi_{\rm Ros} = 56$ mas and $T_{\rm eff} = 3140$ K. Later we consider the implications on the extended atmosphere models of varying these parameters, in particular decreasing ϕ. Values in the literature for $T_{\rm eff}$ for M2 Iab are typically 3500 K (White 1980; Straižys 1992), which would imply $\phi_{\rm Ros} = 46.3$ mas. $T_{\rm eff} = 3140$ K is at the low end of values found in the literature, and its reliability, here, depends on the fidelity of the 11.15 μm ISI visibility data.

To model the 11.15 μm ISI visibility data, which partially resolves the stellar disk and resolves the circumstellar dust

TABLE 3

ADOPTED STELLAR PARAMETERS AND REFERENCE DATA

Quantity	Value	Source
Spectral type	M1–M2 Ia-Iab	Keenan & McNeil (1989)
Parallax	7.63 ± 1.64 mas	Hipparcos & Tycho Catalogues (1997)
Distance	131^{+36}_{-23} pc	Derived
$\phi_{\rm Ros}$	56.0^{+1}_{-1} mas	This work, Bester et al. (1996)
R_*	$789 \pm 172\ R_\odot$	Derived
$E(B-V)$	≤ 0.02	Adopted
g_*	1 cm s^{-2}	Lambert et al. (1984) (uncertain)
$T_{\rm Balm}$	2885 K	This work
$F_{\rm Bol}$	$1.02 \pm 0.06\ 10^{-4}$ ergs cm^{-2} s^{-1}	This work
$T_{\rm eff}$	3140 to >3550 K	Uncertain
Abundances	(Adopted)	
$A_{\rm C}$	2.5×10^{-4}	Lambert et al. (1984)
$A_{\rm O}$	6.3×10^{-4}	Lambert et al. (1984)
$A_{\rm S}$	1.8×10^{-5}	Rodgers & Glassgold (1991)
$A_{\rm Mg}$	4.0×10^{-5}	Rodgers & Glassgold (1991)
$A_{\rm Si}$	3.8×10^{-5}	Rodgers & Glassgold (1991)
$A_{\rm Fe}$	3.4×10^{-5}	Rodgers & Glassgold (1991)
Σ (mean mass per proton)	1.4 proton masses	
$n_e/n_{\rm H}$ (photoionized metals)	$\sim 3.8 \times 10^{-4}$ for $R \gg R_*$	This work
V	+0.40	Adopted F_ν
$U-V$	3.45	Adopted F_ν
$B-V$	1.79	Adopted F_ν
$V-R$	1.07	Adopted F_ν
$V-I$	2.32	Adopted F_ν
$V-J$	3.87	Adopted F_ν
$V-K$	4.40	Adopted F_ν
L	−4.69	Adopted F_ν
M	−4.29	Adopted F_ν

emission, we initially used the photospheric models of Brown et al. (1989). We define the radial scale from $R = R_*$ at $\tau_{\rm Ros} = 2/3$. We fit the 1993 ISI data using an initial extended atmospheric model, including a dust shell, between spatial frequencies of 2–3 $\times 10^6$ rad^{-1}. The $\tau_{11.15\,\mu{\rm m}} = \frac{2}{3}$ surface occurs in the photosphere near where $T_e \sim T_{\rm eff}$. It is well established for late-type main-sequence and giant (class III-II) stars that the IR (2–60 μm) radiation temperature (and hence flux) is a decreasing function of increasing wavelength (Engelke 1992). However, our initial computed photospheric values at 11.15 μm are too high to match the visibility data, a conclusion previously reached by Bester et al. (1996). In order to obtain a fit to the angular size *and* flux, we found it necessary to either reduce the temperature in the upper photosphere or to increase the density scale height within the photosphere, which effectively forces $\tau_{\rm Ros} = \frac{2}{3}$ to occur at greater heights and hence lower temperatures. In any case no combination of $T_{\rm eff}$ and ϕ, with the above photospheric models matches the data. Given the adjustments of the thermodynamic structure required to match the observations, this highlights the need for dedicated photospheric models that include an extended atmosphere. We remind the reader that $T_{\rm eff}$ is only used as a starting guess for lower boundary to the model, whereas the stellar flux distribution is used to determine the dust grain temperatures.

The fudicial inner radius of our model derived from an angular diameter of 56.0 mas, and the *Hipparcos* parallax of 7.63 ± 1.64 mas, is $789 \pm 172\ R_\odot$. Finally, we adopt the element abundances given in Table 1 of Rodgers & Glassgold (1991). The O and C abundances are from Lambert et al. (1984). The adopted stellar parameters and other reference data are collected together in Table 3.

4. THE RADIO OPACITY

The radio opacity is dominated by free-free processes involving electrons interacting with ions or neutral species. A key ingredient in the radio opacity is therefore the electron density or elemental ionization balance. Throughout this paper we are concerned with continuous opacity sources (gas and dust) and the presented model fluxes are for the continuum, i.e., regions free of line opacity. The continuous opacity sources are insensitive to the complex atmospheric velocity fields and enable a robust check on models constructed using UV and optical line profiles.

4.1. *Electron Density*

In the extended atmospheres of evolved late-type stars free electrons are from photoionized metals and from hydrogen via a two-stage process. In order to estimate the electron density, n_e, we first consider the ionization of hydrogen, and then the controlling factors that determine the ionization balance of the metals.

The H $n = 2$ level is excited by electron excitation and resonance scattering in the very opaque H Lyα; the optically thin Balmer continuum then determines the photoionization rate from the $n = 2$ level (see Hartmann & Avrett 1984, hereafter HA84). Briefly, we computed the hydrogen ionization in a fashion similar to HA84 as follows: We adopt a six-level model for hydrogen, with a recombination term included to account for recombination into higher levels (i.e., H I $n > 5$) not explicitly included in the atomic model. We replace the detailed radiative transfer for bound-

bound and bound-free transitions using first-order escape-probability techniques, and solve the statistical equilibrium to obtain self-consistent level populations and optical depths (Rybicki 1984).

The optically thin photoionization radiation fields are represented by fixed rates characterized by radiation temperatures, e.g., $T_{\rm Balm}$, $T_{\rm Pasch}$, etc. We also include the potential effects of wind advection on the hydrogen statistical equilibrium. The role of advection on controlling the ionization balance in the outer wind regions has been stressed by Weymann (1962) and a nice description is given by Glassgold & Huggins (1986). Advection plays an important role when the characteristic rates $R_{\rm adv}$ become large enough to be comparable to the transition rates between different ionization states. Radiative recombination for singly ionized species has typical rates of $R_{\rm rec} \sim n_e \times 10^{-13}$ s^{-1}, while for advection in a spherical flow the effective rate is (see Avrett & Loeser 1992; Glassgold & Huggins 1986)

$$R_{\rm adv} = \frac{1}{n_i}\frac{1}{R^2}\frac{d}{dR}(R^2 V n_i) = \frac{V}{y_i}\frac{d}{dR}(y_i)\,, \qquad (2)$$

where n_i is the population of atomic level i. In the second equality, which is valid when there is a constant mass flux, y_i is the relative population. Our initial model indicates that the likely wind flow velocities reach several kilometers per second over several stellar radii (see below § 8.1), leading to $R_{\rm adv} \ll R_{\rm rec}$.

Since advection does not play an important role in the present analysis of α Ori we defer a discussion of the solution technique to a later paper and neglect advection in the ionization balance of the metals. We adopt a value of $T_{\rm Balm} = 2885$ K based on the GHRS spectra and the ISM and circumstellar reddening model. The observed UV continuum is known to vary by ~40% over a 3 yr period (Dupree et al. 1987), and we caution that there are real uncertainties in the actual UV and FUV radiation field from the unknown interstellar and circumstellar extinction. In our final models the dominant source of free electrons is from photoionized metals and not hydrogen, so the final semiempirical model is not sensitive to the adopted value of $T_{\rm Balm}$.

The low measured CO abundance (Knapp, Phillips, & Huggins 1980; Huggins 1987) and nondetection of SiO (Lambert & van den Bout 1978; Jewell et al. 1991) suggests that molecules are minority species and that elements are predominantly neutral or singly ionized in the circumstellar shell. Haas & Glassgold (1993) detected [O I] 63 μm and [Si II] 35μm emission from α Ori with the Kuiper Airborne Observatory and concluded that O and Si are mostly not in molecular form, but in O I and Si II as suggested by the ionization model of Glassgold & Huggins (1986). Based on these observations we assume that that the majority of metals are either neutral or ionized and not bound in molecules.

The n_e contribution from metals is determined by the balance between photoionization and radiative (rr) and dielectronic recombination. In order to estimate the photoionization rates we need first to evaluate the UV radiation field in the region of interest. Direct observations of UV spectra must be corrected for three potential sources of extinction: (1) ISM, (2) bound-free continua in α Ori's extended atmosphere, and (3) circumstellar dust. Here we do not consider the presence of dust within the chromospheric layers. To estimate the UV radiation field in the radio-emitting region we have used GHRS spectra from 1200–3300 Å (Carpenter et al. 1994a; Carpenter & Robinson 1997) and corrected for the ISM reddening as described above.

To infer the radiation field inside α Ori's dust shell in a fully consistent fashion would require the solution of the full UV anisotropic dust radiative transfer problem. However, in this analysis, we assume that the dust attenuation from α Ori's extended atmosphere can be described by pure absorption with a wavelength dependent effective optical depth given by $\overline{\tau}_{\rm dust} \simeq \tau_{\rm abs}$, where $\tau_{\rm abs}$ is the dust absorption optical depth from the outer envelope.

There are no standard theoretical models of chromospheres, and spatially *unresolved* semiempirical models to date have provided the best estimate for the thermodynamic structure. Consequently the effects of bound-free opacity sources in the extended envelope on the UV radiation field are hard to assess.

The color temperature of the observed UV continuum suggests that Si I λ1521 bound-free continuum is not very opaque above the chromosphere; however, the S I λ1197 edge appears to be quite opaque. It is likely that significant column densities of neutral species exist within the extended envelope. The O I (UV 1) triplet lines at 1303 Å are anomalously weak compared to O I λ1641, which is excited by resonance scattering in the triplet lines. The C I (UV2) lines at 1657 Å are in absorption, whereas they are typically in emission in other stars (Carpenter et al. 1990). Non-LTE computations within a schematic chromosphere suggest that the O I triplet may be absorbed by the Si I bound-free continuum (Carpenter et al. 1994a). Carpenter et al. also note that chromospheric dust, if present, may destroy the resonance line photons. The C I 609 μm transition has been detected confirming the presence of C I in the inner envelope (Huggins et al. 1994; van der Veen, Huggins, & Matthews 1998). The large hydrogen columns in the extended atmosphere of α Ori imply that the C I bound-free edge at 1101 Å may be optically thick even if carbon is mostly in the form C II. There are currently no useful observations below the C I ground state edge to directly address this question. We note that *FUSE* observations will provide vital new information on the FUV region 912–1180 Å. We have estimated the C I column by simulating the circumstellar absorption out of the C I (UV2) lines. Assuming $V_{\rm turb} = 8$ km s^{-1} and $T_e = 2500$ K, and that each intrinsic emission profile in UV2 has the same flux as the corresponding fluoresced C I (UV32) emission lines at 1992.0 and 1993.6 Å. The initial SEM suggests that a column density of $N_{\rm H} \simeq 3 \times 10^{23}$ cm^{-2} overlies the peak in the temperature distribution. Adopting $A_C = 2.5 \times 10^{-4}$, we find that $\overline{\rm C\,I/C\,II} \simeq 0.03$, which implies that, while carbon is mostly singly ionized, the neutral edge at 1101 Å may be very opaque at chromospheric radii. Our estimate for the photoionization rates for C I and S I are based on an extrapolation of the observed UV continuum into the FUV. The photoionization rate for C I is a sensitive function of T_e as the second term (metastable) ($2s^2 2p^2\ ^1D$) has $\Delta E/kT_e = 14665/T_e$ and can be be photoionized by H Lyα.

S I has a ground-state photoionization edge at 1197 Å, and the GHRS spectra shows a strong fall-off in the flux near 1197 Å. If we assume that this decline in flux is a result of $\tau > 1$ at the continuum edge we can obtain an estimate of the neutral sulfur column. Assuming $A_S = 1.8 \times 10^{-5}$ (Table 3), and $\sigma = 1.4 \times 10^{-16}$ cm^{-2} (Tondello 1972), then

$\overline{\text{S I/S II}} \geq 1.3 \times 10^{-3}$. Again large column densities in the SEM predict significant neutral column densities even if the element is mostly singly ionized.

In the absence of a structure model for the hot chromospheric plasma, we approximate the stellar monochromatic mean intensity by

$$J_\nu(Z) = \frac{F_{\nu,\oplus}}{\pi}\left(\frac{2}{\phi_{\rm Ros}}\right)^2 \frac{1}{2}\left(1 - \sqrt{1 - \frac{1}{z^2}}\right), \qquad (3)$$

where $F_\oplus$ is the observed flux corrected for circumstellar and ISM attenuation, z is the normalized radius ($z = R/R_*$), and the last term is the radiation dilution factor. The photoionization rates were computed using this equation and the bound-free cross sections compiled by Mathisen (1984).

We estimated n_e throughout the atmospheric model using the ionization balance between radiative and dielectronic recombination rates from Shull & van Steenberg (1982) and Landini & Monsignori Fossi (1990), and the photoionization rates were estimated from the observed (and extrapolated) stellar UV (and FUV) spectra and estimates of the interstellar radiation field (taken from Glassgold & Huggins 1986). We consider neutral and singly ionized species. We have not solved for the abundance of H_2, which is expected to be a minority species. For low-gravity stars ($\log_{10}[g_*(\text{cm}^{-2}\,\text{s}^{-1})] \simeq 0.0$), however, neutral hydrogen remains the dominant species (Bennett 1991).

For the conditions in α Ori's extended atmosphere we constrained the extrapolation into the FUV so that the S I bound-free edge was opaque at the peak in the T_e distribution while the Si I edge was optically thin. Radiative recombination, which has a mild temperature dependence ($R_{\rm rr} \sim T_e^{-0.7}$), dominates over dielectronic recombination. The fractional contribution for n_e from metals rises quickly above the stellar surface to an almost constant value. The dominant uncertainty is the actual depth-dependent UV/FUV radiation field, which depends on the location of the emitting plasma, and the solution to this problem is far beyond the scope of this paper. If the contribution of electrons from metals is subsequently found to be different by a factor of $f_{\rm met}$ from the values derived above, $n_{\rm H}$ would need to be scaled by $1/\sqrt{f_{\rm met}}$. The photoionization rate is expected to follow changes in the UV/FUV continuum. Since many of the metals including carbon are already mostly singly ionized, modest changes in UV radiation fields will lead to relatively small changes in the electron density. The radio visibility data constrain the SEM inside the dust formation region, and we have not included any reduction in n_e from depletion of metals by dust.

4.2. *Free-Free Radio Opacity*

Hummer (1988) provided Chebyshev fits to the H(free-free) absorption Gaunt factors that are good to $\leq 1.5\%$. In some atmospheric regions $h\nu/kT_e$ lies outside the domain of the Hummer fits; in these regions we use the analytical expression of Scheuer (1960). For the H^-(free-free) opacity we use the fit of John (1988), which reproduce the results of Bell & Berrington (1987) to 1% (John 1994). Below $T_e = 1400$ K we use the approximation derived in Appendix B. For other neutrals, which play a minor role, we scale the opacity from the long-wavelength limits given by John (1975).

It is sometimes convenient to describe the radio opacity in a power-law form for T_e and ν, so that analytical models of different sources can be constructed, e.g., Wright & Barlow (1975), Panagia & Felli (1975), and Olnon (1975). Here we provide an expression for the H^-(free-free) opacity, analogous to that for hydrogenic free-free opacity widely used in the astrophysical literature (given in Mezger & Henderson 1967) and based on an approximation by Altenhoff et al. (1960), i.e.,

$$\kappa_\lambda = \frac{2.12 \times 10^{-1} Z_{\rm ion}^2 n_{\rm ion} n_e T_e^{-1.35}}{\nu^{2.1}}, \qquad (4)$$

where $Z_{\rm ion}$ is the charge of the ion, ν is the radio frequency (Hz), and the particle densities are in units of cm^{-3}.

The atomic negative ion (free-free) opacity (e.g., H^- [free-free], He^- [free-free], O^- [free-free], etc.) at centimeter wavelengths for $1450 < T_e(K) < 6000$, is dominated by neutral hydrogen, but includes contributions from He I and other species which are expected to be neutral, e.g., Ne, N, and O. The opacity can be approximated by the following expression (this work)

$$\kappa_\lambda = \frac{6.20 \times 10^{-11} n_{\rm H\,I} n_e T_e^{+0.22}}{\nu^{2.0}}. \qquad (5)$$

This expression is good to 2.5% for the above T_e-range. After hydrogen, neutral helium is the next major contributor at the couple of percent level. A similar expression can be made for the combined atomic negative ion and neutral free-free opacities with a fixed contribution to the electron density from photoionized metals of $n_e/n_{\rm H} = x_e = 3.8 \times 10^{-4}$:

$$\kappa_\lambda = \frac{6.50 \times 10^{-9} n_{\rm H\,I} n_e T_e^{-0.3}}{\nu^{2.0}}, \qquad (6)$$

which is good to 7% in the same T_e-range.

4.3. *A Simple Circumstellar Silicate Dust Model*

Our calculations also include a simple dust model in order to examine the effects of dust opacity on the UV radiation field which controls n_e and on the IR and radio fluxes. The parameters describing the dust model are given in Table 4. We use the complex dielectronic function for circumstellar silicate grains of David & Pégourié (1995) and extrapolations in the long-wavelength limit. The absorption efficiency $Q_{\rm abs}$ in the long-wavelength limit for this model is $Q_{\rm abs}(\lambda)\lambda^{1.5} = \text{const}$, for which the exponent lies between the values of 1 and 2 expected for amorphous and crystalline grains, respectively (Schutte & Tielens 1989). The adopted dust distribution has a minimum grain size of 0.005 μm and a exponential cut-off near 0.14 μm, which is consistent with the findings of Mauron & Le Borgne (1986) and Jura (1996). We note that Seab & Snow (1989) found from a study of UV extinction of the B-star companion to the M supergiant α Sco that few grains exist smaller than 0.08 μm. It is not clear, however, how the circumstellar environment with the UV bright radiation field from the B star affects the grain size distribution. We compute the absorption and scattering coefficients assuming Mie scattering (van de Hulst 1981; Wickramasinghe 1973). A mean dust temperature ($T_{\rm Dust}$) and opacity was computed for the grain-size distribution. $T_{\rm Dust}$ was computed assuming radiative equilibrium with the stellar flux distribution, which is optically thin in the region of interest.

Since we have fixed the grain size distribution, the complex dielectric constants and therefore the temperature

TABLE 4

ADOPTED CIRCUMSTELLAR DUST PARAMETERS

Quantity	Value
Shape	Spherical
Distribution	$\exp\{-a/a_0\}/a^{3.5}$
a_0	0.14 μm (Jura 1996)
Minimum radius	0.005 μm
Dust density	3.3 g cm^{-3} (Skinner & Whitmore 1987)
Dust-to-gas mass ratio	$f_D = 5.8 \times 10^{-4}$ (this paper)
$\epsilon_1 + i\epsilon_2$	David & Pégourié (1995)
$T_{\rm Dust}$	Optically thin and radiative equilibrium with stellar flux distribution
z_1, σ	33.0, 4.0 (this paper)

for different grain sizes, we vary the dust formation radius and the dust-to-gas mass ratio to match the IR visibility data. We set the dust formation radius by gradually phasing-in the dust opacity κ from the nominal value κ_0 using the following expression:

$$\kappa = \kappa_0 \left\{ \frac{2 \exp\left[(z - z_1)/\sigma\right] + 1 - \exp\left[(1 - z_1)/\sigma\right]}{\exp\left[(z - z_1)/\sigma\right] + 1} - 1 \right\} . \tag{7}$$

This gives the multiplier for the dust absorption and scattering opacity that ranges from zero to unity near a reference radius (z_1) over a normalized e-folding radial distance of σ. This is included to allow for initially incomplete dust formation near the inner surface, and to mimic possible nonexact axial symmetry of the real system. The adopted values of z_1 and σ are given in Table 4. We extend the dust model out to 5′, which is inside the postulated bow shock (Noriega-Crespo et al. 1997).

5. MODELING THE OBSERVATIONS

The centimeter-radio emission from the partially ionized winds of evolved late-type stars can be thought of, to first order, as resulting from an opaque sphere characterized by the temperature and radius (approximately) at a radial optical depth $\tau_{\rm rad} \sim \frac{1}{3}$ (Cassinelli & Hartmann 1977). The specific value of $\tau_{\rm rad}$ depends on the structure of the atmosphere. Owing to the spherical, extended nature of the emission this optical depth is less than $\tau_{\rm rad} \simeq \frac{2}{3}$ characteristic of Eddington-Barbier relations for plane-parallel atmospheres. Since the total source function at centimeter wavelengths is dominated by thermal terms, and not scattering, it is controlled by local thermodynamic conditions. This situation is unlike a resonance scattering line such as Mg II h or k, or H Lyα, where the line source function can be globally controlled by thermodynamic conditions at very large line center optical depths.

The local nature of the radio source term suggests a simple procedure for constructing an initial temperature-density model; starting from the outermost distances where information is available, the model is constructed incrementally in toward the star. Schematically, we start the model by determining the $\tau \simeq \frac{1}{3}$ surfaces for the longest wavelength observation with visibility data (6 cm) using

$$\tau(R) = \int_{\infty}^{R_i} \kappa \, dR . \tag{8}$$

The size of the region is given by the visibilities and the temperature is then set by the absolute flux. Starting with the visibility at 6 cm and the adopted fluxes at 20 and 6 cm, we construct a model for the outer layer with the assumption that the density is smoothly declining outward.

We adopt a hydrogen density distribution, expressed in terms of the normalized radius,

$$n_{\rm H}(z) = \frac{n_{\rm H}^{\rm ext}}{z^2} \left[1 - \left(\frac{0.998}{z} \right)^{\gamma} \right]^{-\beta} + n_{\rm H}^{\rm phot} \exp\left(- \frac{z - z^{\rm phot}}{\alpha} \right) . \tag{9}$$

The first and second terms represent the extended and photospheric components, respectively. The coefficient in the first term (0.998) is a somewhat arbitrary constant chosen to be less than unity to avoid the singularity at $z = 1$. For the photospheric model we initially interpolate the grid of model photospheres given by Brown et al. (1989), and setting $R = R_*$ where $\tau_{\rm Ros} = \frac{2}{3}$. Note that in general $T_e \neq T_{\rm eff}$ at $\tau_{\rm Ros} = \frac{2}{3}$. The photospheric model is used to provide reasonable values of $n_{\rm H}$ close to the star and an opaque boundary condition for the radiative transfer solution. For the first model n_e is taken to be a fixed fraction of $n_{\rm H}$.

To model the layers successively closer to the star, we then consider the next smallest wavelength (i.e with lower opacity) and empirically constrain the optical depth increment, i.e.,

$$\Delta\tau(R) = \int_{R_i}^{R_j} \kappa \, dR , \tag{10}$$

and so on, until we reach 0.7 cm. We continue the model until we reach the radius corresponding to the ISI 11.15 μm measurement. The density between the radii corresponding to 0.7 cm and 11.15 μm is not constrained by visibilities, but nevertheless the mean temperature is chosen to be close to the observed fluxes, which may include dust emission contributions.

Once the initial distributions for $n_{\rm H}(Z)$ and $T_e(Z)$ have been estimated the actual run of $n_e(Z)$ is found from the ionization balance of hydrogen and metals. At this point the radio opacities can be computed. We then solve the spherical radiative transfer problem for the radio and dust and compute the radio and IR visibilities. These are compared to the observations and the parameters describing $n_{\rm H}(R)$ (i.e., α, β, and γ) and $T_e(R)$ are adjusted until satisfactory agreement has been reached.

Such models contain a degree of nonuniqueness, and our choice of the density distribution could bias the semi-empirical model. We feel, however, that this is a pragmatic

approach that amply demonstrates the modeling technique and provides a starting point for future more detailed analyses. For the temperature structure in the outer reaches, where there are no visibility data, we set the temperature to $T_e(R) = T_e(R_{\rm ref})(R_{\rm ref}/R)^{\Gamma}$. The values of $R_{\rm ref}$ and corresponding $T_e(R_{\rm ref})$ were mainly set by the 20 cm flux, and we set Γ to match 38 ± 6 K at 4″ based on the temperature derived from the CO 4.6 μm vibration-rotational lines by Ryde et al. (1999).

The first model we describe is a one-dimensional spherical atmosphere based on all the azimuthally averaged visibility data. This model gives good sizes for the emitting regions and good absolute fluxes. In radiative transfer parlance, one-dimensional is understood to mean that the thermodynamic properties can be specified by a single coordinate, i.e., the radial distance from the center of the star. The radiative transfer problem, naturally includes the full three spatial coordinates. Later we describe a two-dimensional model, described radius and one angle, for the 0.7 cm intensity contours. This model is based on the one-dimensional mean model above but we now let the density and temperature be a function of radius and angle. For the two-dimensional model we write the density (and temperature) as a function of angle

$$n_{\rm H}(r, \theta, \phi) = n_{\rm H}(r)\mathscr{M}(\theta, \phi) , \tag{11}$$

$$T_e(r, \theta, \phi) = T_e(r)\mathscr{M}(\theta, \phi) . \tag{12}$$

In the absence of detailed quantitative spatial information about the three-dimesnsional density structure of α Ori's (see Uitenbroek et al. 1998) we adopt a two-dimensional elliptical model with one axis in the plane of the sky and oriented with a position angle of 67°.5 (east of north). We adopt a form

$$\mathscr{M}(\theta, \phi) = \frac{1}{1 - \eta \cos^2 (\pi/2 - \theta)} , \tag{13}$$

where θ is the angle between the position vector and the plane containing the minor axis; η specifies the degree of density enhancement along the major axis and takes values $0 \leq \eta < 1$.

The radiative transfer problem is then solved for the gas and dust problem, where the total source function is given by

$$S_\nu = \frac{\kappa_{\rm ff} B_\nu(T_e) + \kappa_{\rm abs}^{\rm dust} B_\nu(T_{\rm dust}) + \kappa_{\rm sca} J_\nu}{\kappa_{\rm ff} + \kappa_{\rm abs}^{\rm dust} + \kappa_{\rm sca}} , \tag{14}$$

and

$$\kappa_{\rm ff} = \kappa_{\rm H_{ff}^-} + \sum \kappa_{\rm other\ neutral_{ff}^-} + \kappa_{\rm H_{ff}} + \sum \kappa_{\rm other\ ion_{ff}} \tag{15}$$

is the sum of electron-neutral and electron-ion opacities. The dust source function and opacities are mean values computed for the dust particle size distribution.

$$\kappa_{\rm sca} = \kappa_{\rm sca}^{\rm dust} + \kappa_{ne} \tag{16}$$

is the sum of the coherent dust and electron (Thompson) scattering. We assume all sources of emission are isotropic; for the dominant thermal terms this is a good approximation.

We solve this radiative transfer problem by finding the self-consistent solution for the mean monochromatic intensity J_ν and source function S_ν. For the one-dimensional models we solve the transfer equation along a grid of impact parameters using the Feautrier scheme (see, e.g., Harper 1994). We use an adaptive impact grid which changes the location of the shells with each frequency to optimize the accuracy of the computed values using a finite number of shells. The grid spacing is determined by weighting certain properties, e.g., radius (for angle integration), $\Delta \log \tau$ (for the Feautrier solution), and density and temperature (opacity sampling), which then have a higher density of grid points. These techniques are often used in radiative transfer calculations to optimize computer resources (see Fensl 1995).

The formal solution of the radiative transfer equation gives the specific intensity $I(\rho)$ at a projected angular separation from the center of the star in radians ρ ($\rho_* = \phi_*/2$). The visibilities for the axisymmetric one-dimensional models are given by (White & Becker 1982; Fomalont & Wright 1974):

$$V\left(\frac{d}{\lambda}\right) = 2\pi \int_0^{\rho_{\rm max}} J_0\left(2\pi\rho \frac{d}{\lambda}\right) I(\rho)\rho \, d\rho , \tag{17}$$

where J_0 is the Bessel function of order zero, d is the projected distance between antenna pairs (baseline), and λ is the wavelength. We check the accuracy of the numerical quadratures in the evaluation of the model visibilities by comparing the results of a uniform intensity disk with the known analytical result.

For the two-dimensional model, one of us (GMH) has written a simple and robust three-dimesnsional radiative transfer code based on the method of short characteristics in Cartesian geometry developed by Olson & Kunasz (1987) and Kunasz & Auer (1988). Bilinear interpolation is used for the opacities and source functions, with Gaussian quadrature of nine angles per octant (i.e., 72 angles per unit sphere). In general such three-dimensional codes are known to suffer angular resolution losses and linear interpolation of quantities is somewhat crude. However, at centimeter-radio wavelength the source function is a linear function of T_e, and we are examining large spatial scale variations in density so that for our present application the code appears appropriate. Note also that since the source function is nearly thermal the radiative transfer problem is in this special case simple. In Appendix A we provide benchmarks for evaluating the accuracy of the codes used to solve the current spherical radiative transfer problems. These are also useful for developing analytical models of other sources.

6. THE SEMIEMPIRICAL MODELS

In this section we describe the results of the one- and two-dimensional models.

6.1. *One-dimensional Model*

Figure 2 shows the flux spectrum resulting from the adopted semiempirical model based primarily on the VLA centimeter-radio visibility data, the model fits to the visibility data are shown in Figure 3. Figure 2 shows the spectrum when the simple dust model is included, while Table 5 gives the model fluxes for the model, with and without dust. Figure 4 shows the electron temperature and hydrogen and electron densities as a function of projected radius and angular radius. The temperature in the outer reaches was prescribed using $T_e(z) = 1600.0(5.5/z)^{1.1}$; however, the value of the exponent is not tightly constrained in absence of additional thermal constraints. The hydrogen density is

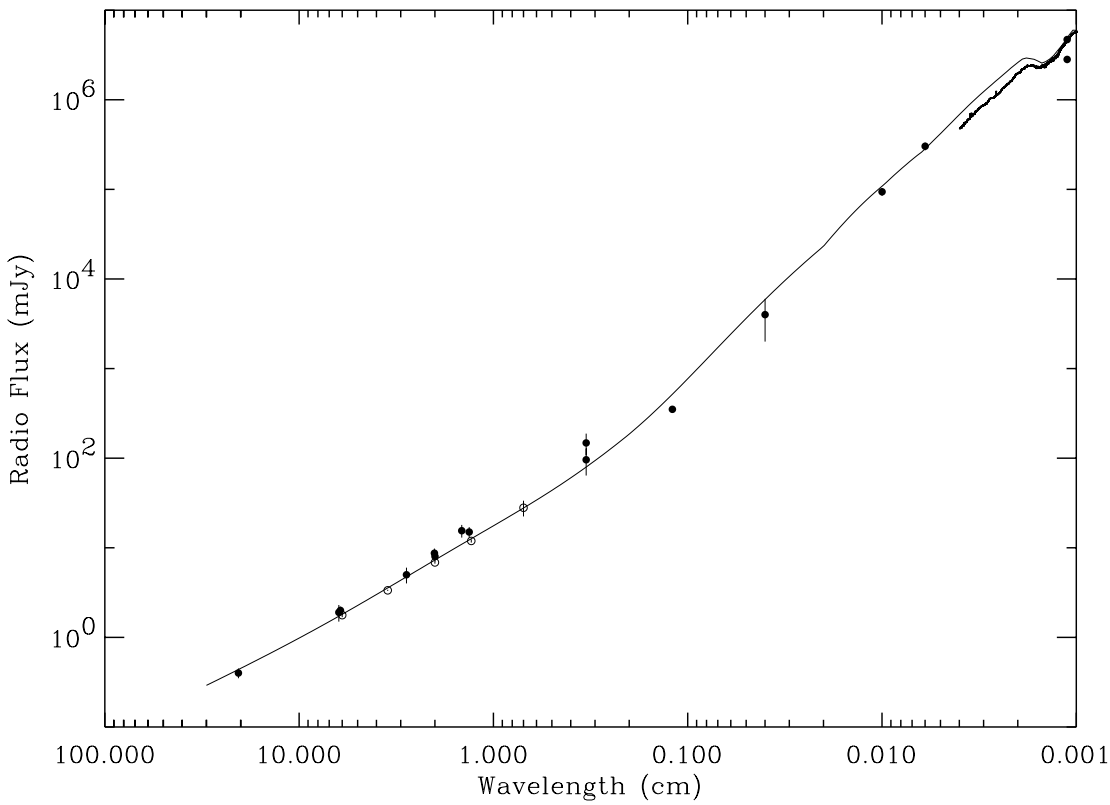

FIG. 2.—Fluxes from the final model (*solid curve*) with data shown from Figure 1. The model gives an excellent fit to the centimeter-radio data, but it is not constrained by spatial information at shorter wavelengths except at 11.15 μm. The dust emission can clearly be seen in the model and *ISO* spectrum.

given by the truncated base photospheric model (eq. [9]) and the coefficients in given Table 6. The one-dimensional model is summarized in Table 7; note that the electron density in the outer layers tends to $n_e/n_{\rm H} \sim 3.8 \times 10^4$.

In Figure 3 the solid line is the one-dimensional SEM and the dotted line is the shape given by a uniform intensity disk model commonly used in the initial stages of visibility analysis. It can be seen that the SEM fits are in good agreement with the Lim et al. (1998) observations where the signal-to-noise (S/N) is good. The dotted line represents a reasonable first approximation to the temperature at the $\tau_{\rm rad} \sim \frac{1}{3}$ surface. This is a result of the density scale height being small compared to the radial distance and the temperature decreasing in the outer part of the atmosphere; however, the uniform disk models do not provide any information on the density structure. To a first approximation we can use the opaque disk description to provide an simple error model to describe the uncertainties in the SEM by

$$\frac{\Delta F_\nu}{F_\nu} = 2\,\frac{\Delta\phi}{\phi(\tau_\nu \simeq 1/3)} + \frac{\Delta T_e}{T_e(K)}\,, \tag{18}$$

noting that the opacity is a weak function of T_e.

The 0.69 cm fit is a compromise between a slightly lower visibility curve and slight overestimate in the integrated flux; this may be the result of the intensity asymmetry. The 3.54 cm flux is slightly higher than observed, and there is a hint that the 6.17 cm data indicates a slightly more extended atmosphere, but given the S/N in the visibility data and the flux constraint from a previous 20 cm flux measurement, the model is an acceptable fit. If we consider the 3.54 cm flux, the SEM overestimates the measured flux by 0.16 mJy, i.e., 5%. To bring the model into close agreement we could either reduce T_e by 5% near the peak of the flux contribution function (see immediately below), or we could adjust

TABLE 5

SPATIALLY INTEGRATED MODEL RADIO FLUXES

Frequency (GHz)	Wavelength	Flux (no dust) (mJy)	Flux (dust) (mJy)
1.46	20.5 cm	0.44	0.44
4.86	6.17 cm	1.75	1.75
8.46	3.54 cm	3.51	3.51
14.94	2.01 cm	7.26	7.26
22.46	1.32 cm	12.2	12.3
43.34	6.9 mm	28.2	28.3
90.00	3 mm	92.2	93.9
250.0	1.2 mm	437.0	516.3
	400 μm	3.33×10^3	5.89×10^3
	100 μm	4.64×10^4	1.08×10^4
	60 μm	1.24×10^5	2.84×10^5
	25 μm	6.57×10^5	1.73×10^5
	11.5 μm	2.77×10^6	4.42×10^6
	11.15 μm	2.93×10^6	4.87×10^6

TABLE 6

PARAMETERS DESCRIBING $n_{\rm H}$

Quantity	Value
$n_{\rm H}^{\rm ext}$	2.50×10^9 cm^{-3}
β	1.10
γ	0.45
$Z^{\rm phot}(R_*)$.....	1.0079
$n_{\rm H}^{\rm phot}$	3.0×10^{14} cm^{-3}
α	0.021

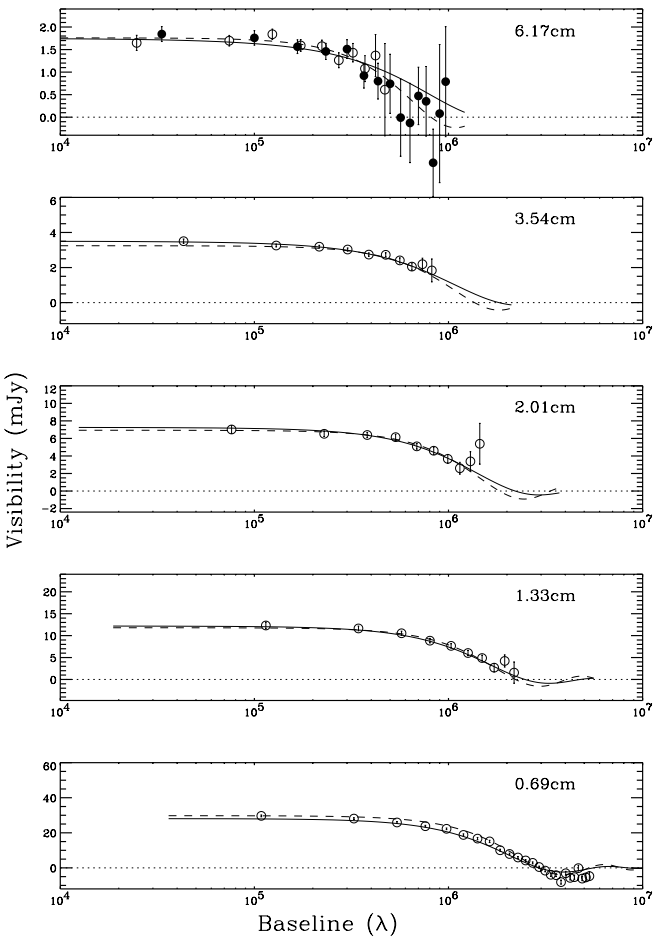

FIG. 3.—Model visibilities for 6.2, 3.6, 2.0, 1.3, and 0.7 cm from the final model (*solid curve*). The observed azimuthally averaged visibilities are shown as hollow circles. For 6 cm the solid circles are the VLA and MERLIN visibilities from Skinner et al. (1997). The dashed curve is the visibility function from the opaque disk model used by Lim et al. (1998). The similarity of the shape of the visibility curves indicates that the opaque disk model is a good starting point for constructing the $T_e(R)$ model.

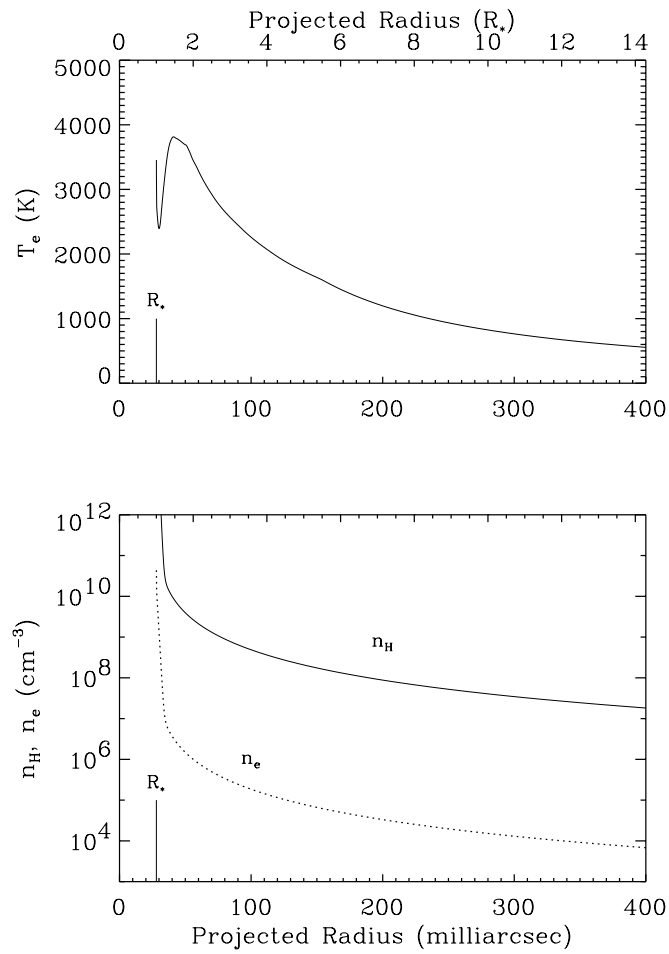

FIG. 4.—Semiempirical model plotted as a function of projected angular (mas) and stellar (R_*) radius. *Top panel:* Electron temperature distribution. Approaching the star from 14 R_* the temperature increases to a maximum near 1.45 R_* and then declines to values below the stellar effective temperature. Finally, T_e increases up toward photospheric values. *Bottom panel:* The hydrogen density is given by eq. (9) and the coefficients in Table 4. Throughout most of the outer model $n_e \simeq 3.8 \times 10^{-4} n_{\rm H}$ (see text for details).

the density structure to ensure that the effective angular diameter is 2% smaller.

Figure 5 shows the relative flux contributions for the radio wavelengths at which we have visibility curves and for the 20 cm datum. This figure provides a concise summary of the spatial information contained in the azimuthally averaged visibility data. This figure shows the relative contribution to the total observed flux from a radius R, i.e., dF/dR of a spherically symmetric source. The flux contribution from a shell with inner and outer radii of R_2 and R_1, of width $\Delta R = R_2 - R_1$, is given by integrating the contribution function from R_2 to R_1. It can be seen that each wavelength has a significant contribution from a range of radial distances. This defines the sense in which our model is a mean model. Intrinsic averaging has occurred over $\Delta R \sim R(\tau = 1)$. The visibilities that we model were first azimuthally summed to increase the S/N ratio. If high S/N visibilities as a function of angle become available, then we could construct models with azimuthal angular resolution. An important point to note is that the depth of the temperature minimum is not well constrained and requires additional constraints such as modeling of molecular line profiles. The 0.69 cm flux has contributions inside the T_e peak of the SEM but becomes opaque above the minimum. In order to assess the nature of the temperature rise above the photosphere, in addition to 0.69 cm visibility data, simultaneous IR observations at wavelengths below 0.69 cm are needed. One device capable of doing this kind of observation is the Submillimetre Common User Bolometer Array (SCUBA), which has detectors which operate between 35 0 μm and 0.2 cm, i.e., in the crucial range.

Figure 6 shows the 11.15 μm visibility model and should be compared to Figure 1 of Sudol et al. (1999) and Figure 2 of Bester et al. (1996). We have adopted the following normalizations for this figure; 4702 Jy at 11.15 μm, and 4490 Jy at 11.5 μm. To obtain a fit at small spatial frequencies, the dust formation occurs near 33 R_*, where $T_{\rm dust} \simeq 360$ K, $n_{\rm H} \sim 3 \times 10^6$ cm^{-3} and $T_e = 220$ K. Alas, this region is not very well constrained by the radio data. The dust-to-gas mass ratio (f_D) was found by matching the flux from the dust shell when the location of the dust formation radius is constrained by the ISI visibility data. We find a value of $f_D = 5.8 \times 10^{-4}$, which is an order of magnitude smaller than the value found for other O-rich (OH/IR and Mira) stars (Knapp 1985), namely, $f_D = 6.3 \times 10^{-3}$, but similar to $f_D = 5 \times 10^{-4}$ found for α Ori by Bowers & Knapp (1987)

TABLE 7

SEMIEMPIRICAL MODEL (SEM)

Radius (R_*)	T_e (K)	Log_{10} (n_{H}) (cm^{-3})	Log_{10} (n_e) (cm^{-3})	Log_{10} (N_{H}) (cm^{-2})	Radius (R_*)	T_e (K)	Log_{10} (n_{H}) (cm^{-3})	Log_{10} (n_e) (cm^{-3})	Log_{10} (N_{H}) (cm^{-2})
1.005.....	2973	14.82	10.33	26.62	1.90.....	3584	9.50	6.08	23.26
1.01.....	2720	14.44	10.07	26.50	2.00.....	3447	9.42	6.00	23.23
1.02.....	2637	14.23	9.92	26.29	2.20.....	3221	9.29	5.87	23.16
1.03.....	2563	14.02	9.77	26.09	2.40.....	3017	9.17	5.75	23.09
1.04.....	2499	13.81	9.62	25.88	2.70.....	2764	9.02	5.60	23.02
1.05.....	2448	13.61	9.47	25.68	3.00.....	2569	8.89	5.47	22.95
1.06.....	2414	13.40	9.32	25.48	3.50.....	2295	8.71	5.29	22.85
1.08.....	2400	12.99	9.01	25.08	4.00.....	2072	8.56	5.14	22.77
1.09.....	2418	12.78	8.86	24.89	4.50.....	1884	8.43	5.01	22.71
1.10.....	2450	12.58	8.71	24.71	5.00.....	1732	8.32	4.90	22.65
1.15.....	2744	11.59	7.95	24.01	5.50.....	1600	8.22	4.79	22.59
1.20.....	3043	10.78	7.29	23.76	6.00.....	1453	8.12	4.70	22.55
1.25.....	3307	10.38	6.93	23.67	6.50.....	1330	8.04	4.62	22.50
1.30.....	3529	10.22	6.78	23.62	7.00.....	1225	7.96	4.54	22.46
1.35.....	3681	10.12	6.69	23.58	8.00.....	1056	7.83	4.41	22.39
1.40.....	3768	10.04	6.61	23.54	9.00.....	926	7.71	4.29	22.33
1.45.....	3811	9.97	6.54	23.50	10.00.....	824	7.61	4.18	22.28
1.50.....	3805	9.90	6.47	23.47	15.00.....	525	7.21	3.79	22.08
1.55.....	3788	9.84	6.41	23.44	20.00.....	382	6.94	3.51	21.94
1.60.....	3771	9.78	6.35	23.41	25.00.....	298	6.73	3.30	21.83
1.65.....	3750	9.73	6.30	23.38	30.00.....	243	6.56	3.12	21.74
1.70.....	3727	9.68	6.25	23.35	35.00.....	205	6.42	2.98	21.67
1.80.....	3688	9.58	6.16	23.31	40.00.....	177	6.29	2.85	21.61

who compared their mass-loss rate derived from H I 21 cm observations with the dust-loss model of (Rowan-Robinson & Harris 1982). The lower dust content in α Ori is consistent with the lower abundance of molecules and higher abundance of neutral species with respect to other O-rich stars. Our value comes from the hydrogen density extrapolated from the SEM, i.e., our estimate for f_D is based on the density ratio and not tied to any specific mass-loss information.

The overall structure of the 11.15 μm visibility curve results from the stellar disk at large spatial frequencies, and the inner edge of the dust forming region at small and intermediate spatial frequencies. Our model is more likely to represent the steady dust shell, as we have not added any extra discrete dust shells. To some extent the amount of "ringing" can be adjusted by changing the σ parameter in the dust model. The present dust model has $\sigma = 4$, which represents a reasonable localized (but not discrete) onset of dust formation. At 33 R_* the adopted density model and the assumption of constant mass-loss rate suggests that the velocity has reached a significant fraction of the terminal wind velocity. Bester et al. (1996) report the onset of new dust emission at 100 mas, which is inside the onset of dust in our model. This region is also near the 6 cm formation region at 3.6 R_*, where the conditions are $T_{\mathrm{dust}} \simeq 1400$ K and $T_e = 2200$ K. If dust formation occurs frequently this close to the photosphere, then simultaneous radio observations would complement IR interferometry.

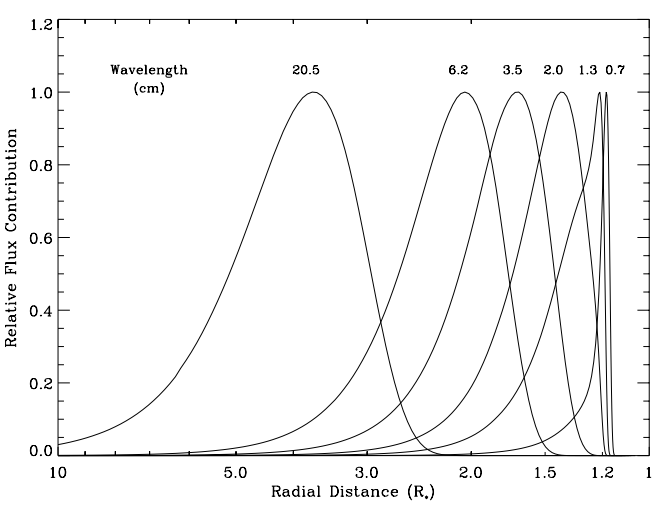

FIG. 5.—Relative contribution functions for the total observed flux. This figure assumes a spherically symmetric source.

Figure 7 shows the spatially integrated continuum fluxes for the SEM computed with and without the dust. For the adopted dust properties this figure suggests that the dust contribution to the total radio flux is negligible at 0.7 cm and longer wavelengths but provides a significant contribution at 60 and 100 μm, and ∼20% at 250 GHz (0.12cm). The flux from the long-wavelength dust emission comes from a very extended region (Rowan-Robinson et al. 1986; Sopka et al. 1985); our model extends to the boundary condition at 5′. The predicted integrated flux depends on the validity of this boundary condition. Comparison of the model with observations therefore also required consideration of the beam width–interferometric observations would resolve out the emission from the largest scales. With the cumulative uncertainties in the dielectric constants, particularly the long-wavelength emissivities, adopted dust grain distribution, or the dust-to-gas mass ratio, it is not possible to be more definitive as to where the dust and radio flux contributions become equal. Future millimeter interferometric observations will be valuable in this respect, e.g., with the Atacama Large Millimeter Array.

On the basis of the steady visibilities at smaller spatial frequencies, Sudol et al. (1999) propose that there is steady

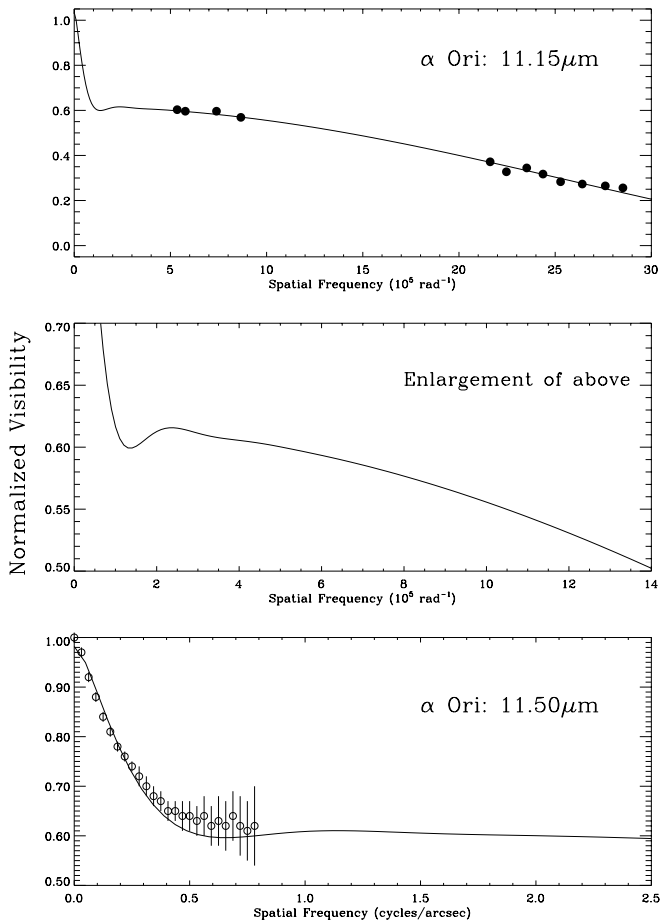

FIG. 6.—11.15 μm visibility curve for the adopted circumstellar silicate dust model. This figure can be compared with Fig. 2 of Bester et al. (1996) and Fig. 1. of Sudol et al. (1999). For ease of comparison with these references the axes are not the same in all panels. The total flux at 11.15 μm is 4702 Jy.

mass loss with episodic bursts, which lead to dust density enhancements. This picture is more consistent with our findings, than a model based on a limited number of discrete shells (Danchi et al. 1994). Sudol et al. (1999) also draw attention to the need for multiepoch observations which contemporaneously resolve both the disk and the extended emission. A complete dust model will need to allow for both α Ori's observed time-dependent, nonsmooth structure, and its multiwavelength behavior. To investigate the degree of ringing in the IR visibility curves we compute two additional models with different values of $\sigma = 2,4,6$ at $z_1 = 33$, which are shown in Figure 8. The model curves are assumed to have exact azimuthal symmetry, which is unlikely to occur in nature. It is more likely that interferometry measurements at one position angle will show more ringing than observations based on azimuthally averaged data. Our model curves do, however, suffer some smoothing from the discretization of the impact grid. In the models shown the number of depth points generated by the adaptive grid that lie within $\pm 1\ \sigma$ of z_1 for each σ are, in parentheses, $\sigma = 2(5)$, $\sigma = 4(10)$, $\sigma = 6(14)$.

6.2. *Two-dimensional Model*

The 0.7 cm data show departures from axial symmetry in the intensity distribution near the surface of the star. An elliptical disk fit gives 95 ± 2 mas by 80 ± 2 mas with a position angle of $67° \pm 7°$ (Lim et al. 1998). The intensity contours are shown in Figure 9*a*.

To investigate whether the asymmetry is most likely a result of density or temperature asymmetries, we have constructed a two-dimesnsional model in which the atmospheric properties are described on ellipsoidal surfaces. The atmospheric properties are characterized by a sector model, where the density and opacity is enhanced along one axis relative to the perpendicular plane. The one-dimensional SEM derived above was scaled in radius and taken to represent the equatorial plane (minor axis), while $n_{\rm H}$ or T_e are enhanced along the major axis. In the absence of additional information, we assume that the major axis lies in the plane of the sky. In this way if the enhanced emission is actually tilted toward the observer, the inferred asymmetry is a lower limit. The hydrogen ionization model described below in § 8.4 was used to derive n_e, with a constant contribution of $n_e/n_{\rm H} = 3.8 \times 10^{-4}$ from the photoionized metals. The resulting map of specific intensities was convolved with the restoring beam of the VLA 0.7 cm observation.

We attempted to fit the intensity contours to the overall shape of the observed contours, rather than the fine structure, because the absolute confidence of the individual contours is not high. The absolute photocenter is not well enough determined to ascertain how well the optical and radio images are coaligned. Reasonable fits had a density enhancement factor of $\eta = 0.95$, i.e., a peak density contrast of 20. Figure 9 (*top center*) shows the intensity from this model, and below (*bottom center*) shows the same model but where we have rescaled the density to approximate the observed total radio flux. If we were to attribute this to an enhancement of mass loss along the major axis, then the integrated stellar mass loss would be ~ 2.6 greater than the mean one-dimensional model. This modest increase in the total mass-loss results from the renormalization of the density scale required to give the correct total flux. This insensitivity to the total mass-loss rate was noted by Schmid-Burgk (1982).

The effects of changing the temperature scale are much more dramatic. The thermal source term is larger and if hydrogen becomes ionized the wind opacity increases almost exponentially. Figure 9 shows temperature models with $\eta = 0.5$ and $\eta = 0.67$, a peak temperature contrast of 2:1 and 3:1 here we have *not* renormalized the T_e scale to give the observed flux. The $\eta = 0.67$ model is clearly too extended, while the $\eta = 0.50$ is a reasonable fit. Previous quantitative models of the large-scale structure, e.g., 10″ of Betelgeuse, based on imaging observations suggest the density is reasonably symmetric, e.g., Le Borgne, Mauron, & Leroy (1986) did not find dust inhomogeneities greater than a factor of 2. Hα images are also reasonably symmetric to first order. This suggests that if the asymmetry in the 0.7 cm intensity contours was due to an increase in mass loss into a particular solid angle, then it is not steady, or, more conservatively, it results from a combination of density and temperature asymmetries. Tighter constraints on the asymmetries will require higher spatial resolution and S/N observations.

6.3. *Sensitivity to Adopted Stellar Angular Diameter*

The one-dimensional model described above is essentially unchanged in the centimeter-radio emission region under a change of assumed ϕ_* or R_*. Since there is some uncertainty in ϕ_*, with some estimates being somewhat

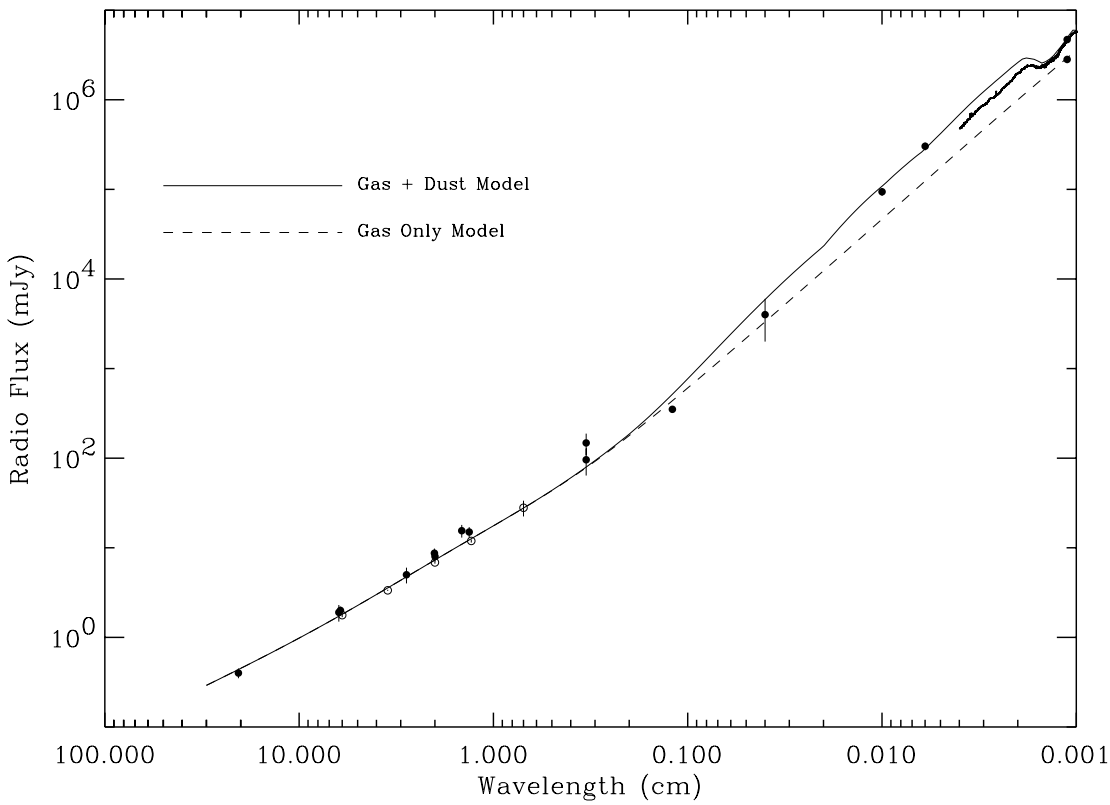

FIG. 7.—Continuum fluxes computed from the SEM. The solid curve is the same as shown in Fig. 2; the dashed curve shows the same SEM, but with the dust removed. This figure illustrates the estimated contribution to the overall fluxes from the dust shell.

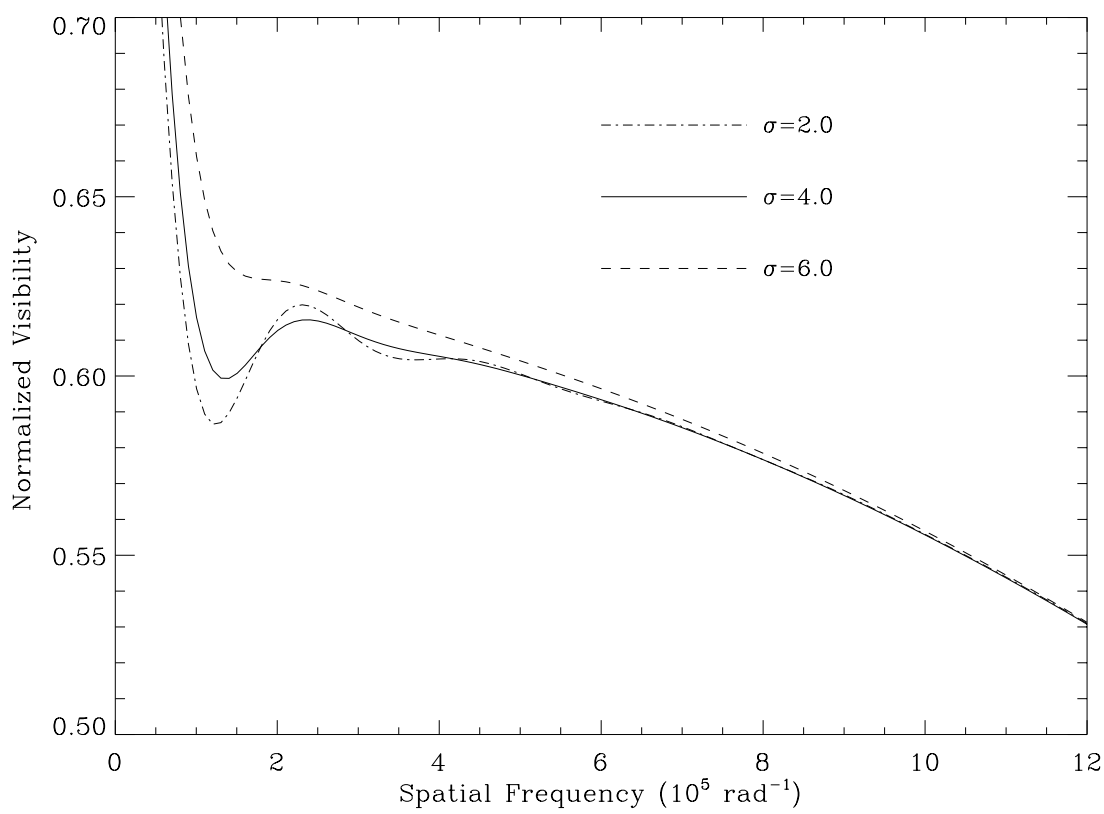

FIG. 8.—Ringing in the 11.15 μm visibilities as a function of model shell sharpness parameter $\sigma = 2, 4, 6$, at $z_1 = 33$ (see text for details)

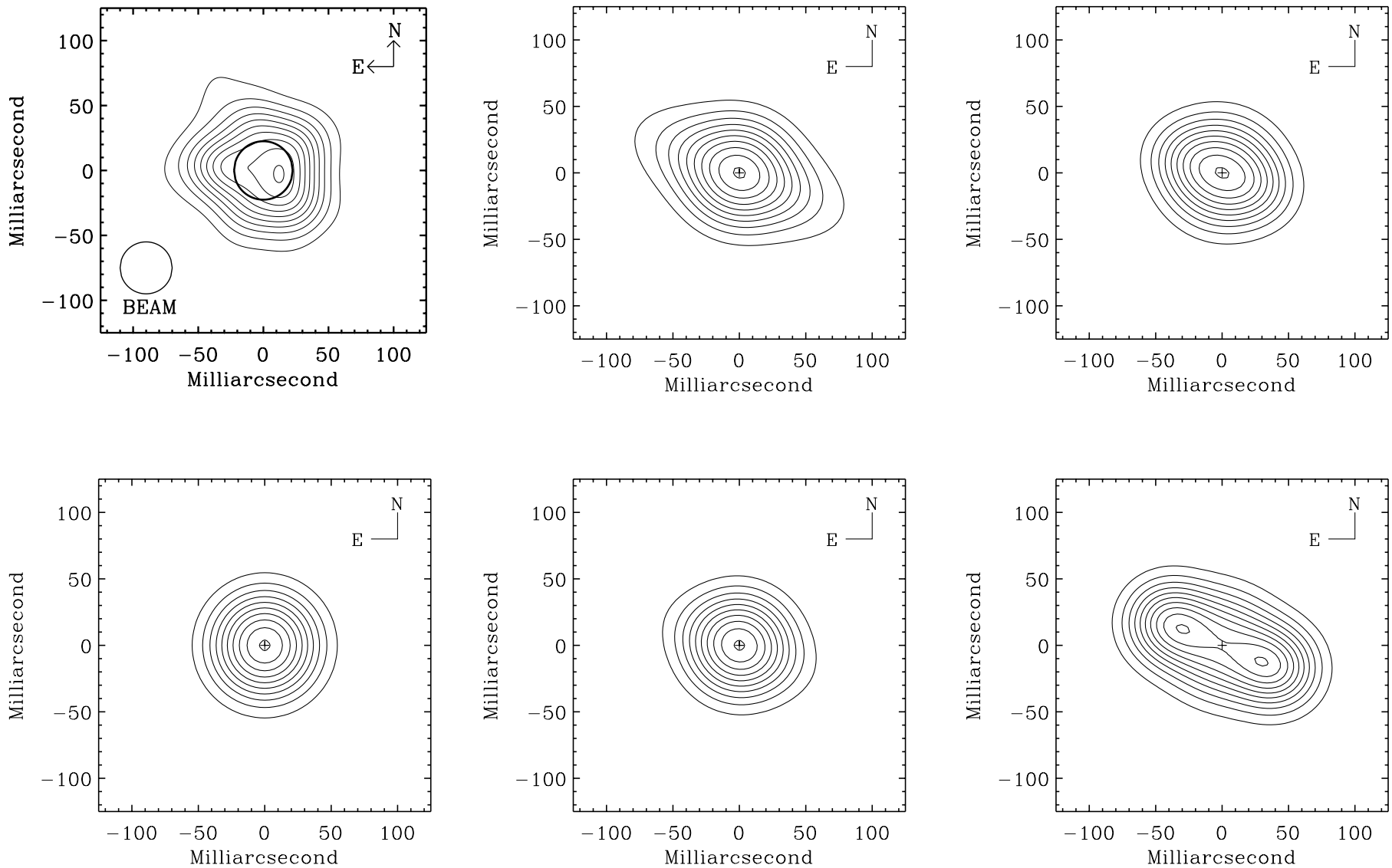

FIG. 9.—Intensity contour maps for 0.7 cm from the two-dimensional models described in the text. In all panels the contours are at 99%, 90%, 70%, 50%, 30%, and 10% of peak intensity. The two-dimensional models was designed to match the overall degree of asymmetry rather than the more complex curves seen in the 20% contours, which have a lower level of significance. *Top left:* Reconstructed intensity map from Lim et al. (1998). *Bottom left:* Spherical model with no asymmetries. *Top center:* Hydrogen density asymmetry model with $\eta = 0.95$. This figure has not been renormalized to give the same total radio flux. *Bottom center:* Hydrogen density asymmetry model with $\eta = 0.95$ and the density scale renormalized to give original radio flux. *Top right:* T_e asymmetry model with $\eta = 0.50$ (unnormalized). *Bottom right:* T_e asymmetry model with $\eta = 0.67$ (unnormalized). While smaller T_e asymmetries can lead to observable asymmetries, the present data cannot rule out a more extreme local density asymmetry, or a combination of both.

smaller than 56 mas we consider what changes in the SEM would result from a reduction in ϕ_* Since we are constructing a semiempirical model from the radio visibility data and we are assuming that the distance to the star is known, the primary requirement is that we maintain the same temperature and density structure as a function of projected angle in the sky. In this case the spatial and density scales remain fixed, and therefore the opacity scale given by equation (8) is also constant. Note that this would not be true in general if we had adopted a new distance to the star. The rather uncertain region above the photosphere would need to be adjusted, and a new photospheric component added since this region is not in the original model. The new implied $T_{\rm eff}$ resulting from a new ϕ_* is not relevant as $T_{\rm eff}$ is not used directly, since we are unable to match a photospheric model to the ISI data. The chromospheric radiation field is constrained by UV observations (where possible). Since n_e is controlled by photoionization from the chromospheric radiation field then for a given projected angular distance from the star J_ν from equation (3) is only slightly changed. Differences of order 10%–20% will occur near the temperature minimum region because the radiation dilution factor in equation (3) does not scale as R^{-2} for $R \simeq R_*$.

The main difference in the SEM would be in the modeling of the ISI 11.15 μm visibilities. Our initial trial photospheric model was unable to reproduce the size and flux of the stellar component. We drastically altered the $n_{\rm H}$ structure near $z = 1.0078$ with a density scale height (H_ρ) of $H_\rho/R_* \simeq$ 2%. The observed H_ρ in the lower chromosphere of the intermediate mass primary in the eclipsing binary ζ Aurigae is $H/R_* = 2\%$ (Schröder, Griffin, & Griffin 1990); however, it is not clear that such nonthermal scale heights are really present so deep in the photosphere of Betelgeuse. If we adopted a smaller photospheric angular diameter, then we would need to drastically increase H_ρ and/or the density where the scale height becomes nonthermal. Since our model does not address the photospheric structure except through the ISI data we do not pursue this point. The onset radius of the dust shell is again determined by the observed IR angular scale. *To summarize: to first order the one-dimensional SEM described in the previous section can be adapted to different stellar radii by mapping the thermodynamic quantities to maintain the same projected angular scale.*

7. CONTROLLING PHYSICS

Our mean semiempirical models do not contain regions of significant hydrogen ionization and the radio opacity is controlled by the n_e contribution from singly ionized metals. The main uncertainty in the density model is from the abundance and ionization of carbon. The metals with first ionization potential less than 13 eV are mostly singly ionized, so n_e is not very sensitive to small uncertainties in the UV photoionization radiation field. Under the conditions in the SEM the dominant radio opacity is from H^- (free-free), which is a neutral-electron interaction. This opacity source is also thought to dominate the centimeter-radio emission from Miras (Reid & Menten 1997). Glassgold & Huggins (1986) showed that when the mass-loss rate gets much above 10^{-6} $M_\odot$ yr^{-1} advection ceases to be important for the hydrogen ionization in the outer wind flow. Our estimate of the mass-loss rate (see below) is greater than this and, as the flow velocities are still small, advection of ionized hydrogen is unimportant for the conditions in the radio-emitting region.

Spectral indices, typically constructed using observations at two or more different frequencies, are often used to infer properties of stellar winds. α Ori's SEM allows us to examine in detail the properties responsible for the observed slope in the radio continuum. Most previous studies of radio emission from "noncoronal" evolved late-type stars have assumed that the dominant opacity is H(free-free) (ion-electron interaction). Analytical work typically utilized a power-law representation of the opacity source and gives the well-known results of a spectral-index $\alpha = 0.6$ for a wind with constant temperature, ionization fraction, and velocity. As one approaches the star the density scale-heights decrease and the spectral index approaches the limit of a blackbody opaque disk, namely, $\alpha = 2.0$. We have made, albeit crude, power-law fit for the opacity of H^-(free-free) and for a mixture of both H^-(free-free) and H(free-free) corresponding to $n_e/n_{\rm H} = 3.8 \times 10^{-4}$ (See Appendix A). At centimeter-radio wavelengths the frequency dependence is similar for all opacity sources ($\kappa \propto \nu^{-2}$), while they have quite different electron temperature dependencies. We note that the H^-(free-free) does not entirely dominate over the whole temperature range; at lower T_e where hydrogen is almost totally neutral, free-free opacity from photoionized metals becomes important.

If we represent the atmospheric properties, such as the hydrogen density, electron temperature and density, ion density, and charge as different power laws in radius, e.g., for a quantity $x(R)$ with index ω,

$$x(R) = x(R_o)\left(\frac{R_o}{R}\right)^{\omega}, \tag{19}$$

then as long as the radial optical depths at R_o are sufficient to shield the underlying photosphere, this analytical model gives a constant spectral index given by (see Appendix A for details)

$$S_\nu \propto \nu^{\alpha}. \tag{20}$$

If the power-law indices for the relevant thermodynamic quantities are given by ($n_{\rm H}$:q), (T_e:d), ($n_e/n_{\rm H}$:b), ($n_i/n_{\rm H}$:a), and ($Z_{\rm ion}$:c), with the opacity per n_e, per interacting particle n_i, having the form

$$\kappa \propto \nu^f T_e^t, \tag{21}$$

then the constant spectral index is given by

$$\alpha = \frac{2a + 2b + 4c + 4q - 2 + 2t \times d + 2 \times f - d \times f}{a + b + 2c + 2q + t \times d - 1}. \tag{22}$$

A crude power-law fit to the semiempirical T_e and $n_{\rm H}$ structure outward of 1.8 R_* gives $T_e \propto R^{-0.74}$ and $n_{\rm H} \propto R^{-2.85}$. For the conditions in the atmosphere we can take $a = b = c = 0$, $d = 0.74$, and $q = 2.85$, and together with the *mixture* opacity model, this gives $S_\nu \propto \nu^{1.44}$. If the dominant opacity had been solely H^-(free-free) then $S_\nu \propto \nu^{1.48}$. If H (free-free) opacity dominated, for example in a warm wind of a hybrid bright giant, e.g., (Harper et al. 1995), then for the same power-law model we would have $S_\nu \propto \nu^{1.28}$. The difference in spectral index is quite small, especially given the typical S/N of observations and the different wavelengths used to construct an empirical spectral index (see, e.g., Drake & Linsky 1986; Drake, Linsky, & Elitzur 1987). In order to use empirical spectral indices to constrain stellar atmospheric models, it is imperative that simultaneous high

S/N observations are made at as many wavelengths as is feasible.

8. DISCUSSION

Previous wind models, dating back to Wischnewski & Wendker (1981), have assumed α Ori possesses a warm wind with partially ionized hydrogen as a source of electrons. Essentially, this and other models required an extended atmosphere at chromospheric temperatures in order to reproduce the observed radio fluxes. Without any knowledge of the actual size of the emitting region the choice between a warm and extended structure, and a cooler and slightly more extended structure was unconstrained.

The direct observation of the radio size, e.g., Lim et al. (1998), showed that the gas is indeed cool, much less ionized, and somewhat more extended. Perhaps the key to the stark contrast in these two pictures of α Ori's atmosphere lies in the fact that when the wind cools the hydrogen ionization falls very rapidly and the H(free-free) opacity becomes small. However, the presence of electrons from photoionized metals and the opacity from H^-(free-free) is sufficient to provide the observed radio emission. The VLA visibilities have provided us with the crucial spatial information. Given that the radio emission from α Sco (M1 Iab) has a similar spectral index, there is clearly a wider applicability for the implications of the current model. Now we have a model for the n_H, T_e, and n_e we are in a firm position to consider other observational diagnostics formed in the region covered by the radio data.

8.1. Fe II *Emission-Line Profiles, Velocity Information, and Mass-Loss Rates*

At this point, the SEM is not based on any specific velocity information. If we could estimate the wind velocity at a particular radius then we could estimate the mass flux at that radius. In previous studies of evolved late-type stars, e.g., γ Cru (M3 III) (Carpenter, Robinson & Judge 1994) and λ Vel (K4 Ib) (Carpenter et al. 1999), clear relationships were found between relative line optical depth in the self-reversed UV Fe II emission lines and the velocity of the wind absorption feature. These observations clearly demonstrated that the winds are accelerating above the surface of these stars. Carpenter & Robinson (1997) obtained *HST*/GHRS observations of α Ori in 1992 September 22 and 24, but found a less clear trend compared to other stars when they considered all the Fe II lines. However, when they examined only the stronger lines, i.e., those with a branching ratio greater than 0.05 they found the same characteristic wind acceleration seen in the other two stars.

The SEM provides $n_H(R)$, so we can estimate the local mass-loss flux for each of the stronger lines by determining the radius where the optical depth ($\tau_{\Delta V}$) at the observed wind absorption feature is unity. We then have $n_H(R)$ corresponding to V_{abs} and a mass-loss rate given by

$$\dot{M}(R) \simeq 4\pi R^2 \Sigma m_p n_H(R) V_{abs} , \quad (23)$$

where Σ is the mean mass per particle. To compute $\tau_{\Delta V}$, where the wind absorption feature appears at ΔV in the observer's frame, we use the SEM and assume that, Fe II is the dominant ionization stage, a microturbulence equal to the 1.5 times the local sound speed, and the full non-LTE level populations for Fe II are computed using escape probability techniques.

We considered the lines with a branching ratio greater than 0.05 and that are thought to be unblended. If we make the additional assumption that the mass-loss rate is steady and constant with radius, we find $\dot{M} = 3.1 \pm 1.3 \times 10^{-6}$ $M_\odot$ yr^{-1}. Part of this scatter results from uncertain absorption oscillator strengths and measurement error. Possible systematic uncertainties in this value, and not included in the error estimate, may result from (1) changes in density structure between the times of the VLA and GHRS observations, (2) errors in the adopted C abundance and ionization balance, (3) errors in the assumed the Fe II/Fe I ionization balance, and (4) the modeling of the Fe II wind absorption features, namely, the assumed microturbulence. The mass-loss rate is unlikely to be more than a factor 2 greater than that given above since the Fe II wind absorption velocities range from $1 \rightarrow 6$ km s^{-1} in the rest frame of the star, and this is a significant fraction of the 11 km s^{-1} circumstellar absorption velocity observed in CO at 4.6 μm (Bernat et al. 1979). This estimate of the mass-loss rate is about a factor of 3 greater than the more recent published values when they are corrected for the new *Hipparcos* distance; e.g., Bowers & Knapp (1987) obtained $\dot{M} \sim 1 \times 10^{-6}$ $M_\odot$ yr^{-1} using VLA H I λ21 cm line observations. Guilain & Mauron (1996) obtain the same value from circumstellar K I scattering observations. This similarity in mass-loss rate is very suggestive that the SEM includes the all important wind acceleration region.

The approximate wind velocity law can also be found from the continuity equation, assuming that the estimate for $\dot{M}$ is the same for all radii:

$$V(R) = \frac{\dot{M}}{4\pi \Sigma m_p R^2 n_H(R)} . \quad (24)$$

This velocity model is shown in Figure 10.

Analysis of circumstellar lines by Weymann (1962) led to a circumstellar model where $N_H \sim 10^{22}$ cm^{-2} and an electron temperature of order 1000 K. There is considerable uncertainty in these parameters, but at this column density our model has $R = 12.8$ R_* and $T_e = 1000$ K. However, Bernat (1977) derived a significantly larger radius 50 R_* for $N_H = 1.3 \times 10^{22}$ cm^{-2}, leading to a larger mass-loss rate of

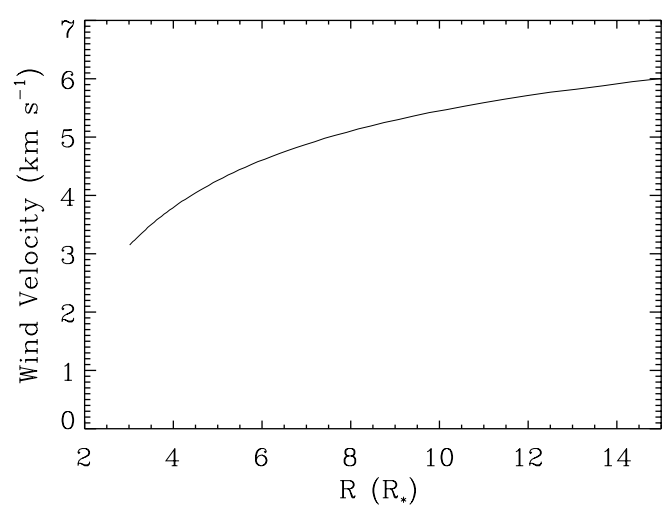

FIG. 10.—Velocity structure inferred by mass conservation in a spherical flow. The velocity can be negative (downflow) or positive (outflow). The presence of weak outflow signature in UV Fe II emission lines suggest the flow is of a positive sign.

$3.4 \times 10^{-5} M_\odot$ yr^{-1}, while Sanner (1976) found an inner shell radius of $\sim 4\ R_*$ and $\sim 2.2 \times 10^{-7}\ M_\odot$ yr^{-1}). When the wind has reached its terminal flow speed, the hydrogen column density is proportional to the radius, i.e., $N_{\rm H}(R) \propto R$, so that any uncertainty in the column density can lead to significant uncertainty in R. A reexamination of these earlier results and the calcium ionization balance in α Ori is planned with upcoming *FUSE* spectra.

8.1.1. *A Note on the* Fe II *Profiles*

Boesgaard & Magnan (1975) and Boesgaard (1979) used spectra of Fe II multiplets 1, 6, and 7 (3150–3300 Å) obtained between 1970 and 1975 to construct schematic atmospheric models for Betelgeuse. These self-reversed line profiles frequently showed the blue emission peak brighter than the red. Using radiative transfer calculations they showed that the Fe II line profiles could be explained as a result of infall of gas in the region within 2.5 R_*.

The radio density model itself is not sensitive to the velocity fields in α Ori's atmosphere, and cannot distinguish between outflow or infall. However, if we assume that the atmospheric structure in the 1990s was similar to that in the period 1970–1975, based on the similarity of the centimeter-radio fluxes, then we might expect that the mean density structure was similar at these times (see § 8.1). In the discussion above we found that if we imposed a steady outflow combined with wind velocities from GHRS Fe II absorption features, we derive a mass-loss rate which is similar to several independent studies. The 3150–3300 Å spectral region and later *IUE* Fe II spectra (Carpenter 1984) actually showed a mixture of profiles with lines showing both red and blue asymmetries. The Fe II line profiles and the associated velocity flows are an intriguing problem. The process responsible for the unusual profile asymmetries remains unknown and is currently under investigation.

8.2. *Previous Atmospheric Models*

Before proceeding, we should address a couple of issues regarding previously published models of α Ori that have utilized radio data. The theoretical constant damping length, Alfvén wave–driven models of HA84 were found to overestimate the radio emission in the 2–4 R_* region, which implied that their model electron densities were about a factor of 2 too large. Their model broadly reproduces the observed off-limb Hα intensities (Hebden et al. 1987; Christou et al. 1988). HA84 adopt an angular diameter of ~54 mas so that spatial scales as projected on the sky are similar to our model. Note that the blackbody photospheric contribution in their Figure 3 appears to be a factor of ~3 too small, giving the impression that the extended atmosphere gives a greater flux contribution relative to a naked photosphere than it actually does. The HA84 model has been a most useful reference tool in the absence of detailed semiempirical models.

The detailed semiempirical model of Skinner et al. (1997) combines both radio and mid-infrared images. We find that their VLA/MERLIN 6.0 cm visibility data agree with those obtained by Lim et al. (1998). Their chromospheric model is somewhat warmer than ours. We have computed centimeter radio fluxes using their semiempirical $n_e(R)$, $n_{\rm H}(R)$, and $T_e(R)$ model and find that the fluxes appear to be about a factor of 3–4 too large, We are, at this time, unable to explain this discrepancy, and consequently we were motivated to provide the benchmark given in Appendix A. Note that our code reproduces well the centimeter wavelength fluxes shown in Figure 3 of Hartmann & Avrett when their model (HA84 Table 2) is used. Figure 11 shows a comparison of our T_e model as projected on the sky (in mas) with both HA84 and Skinner et al. (1997). Clearly our mean radio model is much cooler in the wind acceleration region.

8.3. *Emission from an Inhomogeneous Chromosphere*

Optical and UV spectra show the presence of chromospheric plasma where photons of Ca II, Mg II, and Fe II are created. These lines require hydrogen to be much more ionized than the cool extended atmosphere observed in the radio. Consequently chromospheric plasma will also be much more opaque to the radio making the warmer plasma potentially more visible. One can ask the question, at what radial distances is this plasma present, and under what conditions should it be detectable?

The problem of drawing firm conclusions about the nature of the inhomogeneities is orders of magnitude more difficult than for a single mean model.

The radio source function is proportional to T_e so that chromospheric plasma with $T_e \sim 8000$ K can be concealed if the areal filling factor (AF) is small. For example, if the ambient temperature is say $T_{\rm amb} \simeq 2000$ K at $R = 1.45\ R_*$ and $T_{\rm chrom} = 10{,}000$ K, then for an inferred average of $T_e = 4000$ K, then AF($1.45R_*$) $\simeq \frac{1}{4}$. The thermal averaging inherent in the radio continuum observations does not provide us with information about possible hot plasma with a very small volume filling factor. As the SEM was also computed under the assumption of steady state we may be sampling an average of many dynamical events whose individual properties are different from the mean.

Chromospheric densities deduced from low opacity C II] UV0.01 n_e-sensitive multiplet at 2325 Å indicate $n_e \sim 10^{8.3}$ cm^{-3} (Judge & Carpenter 1998), which is significantly greater than that in the theoretical model of HA84. This suggests that either the chromospheric emission originates in the deeper layers close to the star or in condensations that are highly clumped in a lower ambient density plasma. Judge & Carpenter (1998) also tentatively find that different UV0.01 flux ratios give consistent n_e if the mean hydrogen

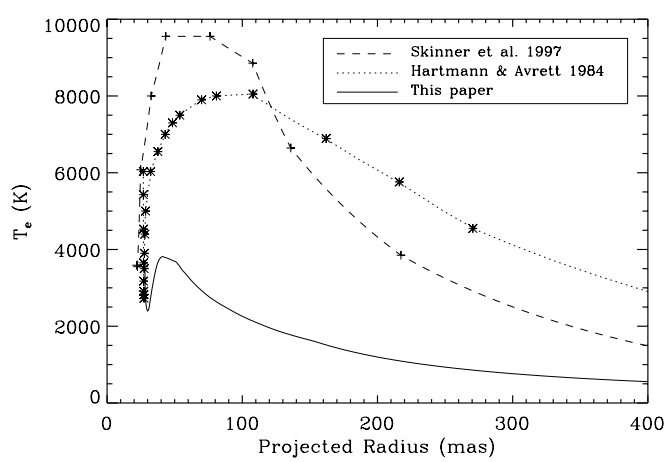

FIG. 11.—Comparison of electron temperatures from different models of α Ori. We have taken the projected angular scale corresponding to each reference, but have not attempted to correct for changes in assumed stellar parameters. The symbols mark tabulated point and the lines are intepolations to guide the eye. The temperature structure implied by the VLA visibilities is noticeably cooler than previous models.

column density of the emitting region of the C II] flux has $N_{\rm H} \sim 3 \times 10^{23}$ cm^{-2}. Under these conditions the strongest lines in the C II] UV0.01 multiplet, which are expected to be optically thin in giant star chromospheres, will become slightly opaque. This hydrogen column density would place the C II UV0.01 line-forming region near the peak T_e of the SEM. Therefore we tentatively identify the peak in temperature distribution with the dominant chromospheric emission region.

The *HST* FOS observations of Dupree et al. (1987) show a narrowband UV source about twice the photospheric angular diameter. The high column densities in the atmosphere provide a very efficient source of line scattering. The optical depths in the Mg II *h* and *k* and numerous Fe II lines are very large. One explanation for the observed extent is that the original source of the photons is not *very* extended, say, $R \simeq 1.45\ R_*$, but the line radiation scatters in an even more extended region, giving the appearance of a very extended disk in the strong scattering lines. The GHRS scans of the Mg II h & k region described by Uitenbroek et al. (1998) are consistent with this picture, but a detailed comparison is needed.

8.4. *Schematic Models*

Using a simple analytical description of the excitation and ionization of hydrogen, which follows closely HA84, we can explore potential effects of temperature inhomogeneities within the extended atmosphere. Since the atmosphere is dominated by neutral hydrogen, most H atoms will be in the ground state. The population of the $n = 2$ level is given approximately by

$$\frac{n_1}{n_2} \simeq \frac{A_{21}/\tau_{21} + C_{21}\, n_e}{C_{12}\, n_e}\,, \tag{25}$$

where C_{12} is the excitation rate from $n = 1$ to $n = 2$ and can be approximated near 5000 K by

$$C_{12} = \frac{8.65 \times 10^{-7}}{T_e^{0.36}} \exp\{-h\nu/kT_e\} \tag{26}$$

using a simple power-law fit to the collisional excitation rate of Scholz & Walters (1991). An estimate for the line center radial optical depth in H Lyα is given by

$$\tau_{21} \simeq 7.6 \times 10^{-13}\, \frac{N_{\rm H}}{\Delta V}\,, \tag{27}$$

where ΔV is the most probably velocity of the small-scale atmospheric motions (turbulence) in kilometers per second. We adopt $\Delta V = 6$ km s^{-1}. If hydrogen is mostly neutral in both background and warm gas phases, then $N_{\rm H}$ taken from the mean model should remain a good estimate of the overlying neutral hydrogen column density. An implicit assumption in this model is that the single-flight escape probability can be written as $1/\tau_{{\rm Ly}\alpha}$, where we have used the static optical depth neglecting velocity gradients. We note that detailed calculations are needed to quantify the accuracy of the above expressions, especially in light of the inhomogeneous nature of α Ori's atmosphere.

An estimate for the ratio of $n = 2$ to the proton density (n_κ) assuming that the Lyman continuum is optically thick can be written

$$\frac{n_2}{n_\kappa} \simeq n_e\, \frac{3.3 \times 10^{-14}}{W(z)}\, \frac{\exp\{I_2/kT_e\}}{T_{\rm Balm}\, T_e^{0.34}}\,, \tag{28}$$

where $T_{\rm Balm}$ is the radiation temperature that characterizes the optically thin photoionizing Balmer continuum of energy I_2, $W(R)$ is the radiation dilution factor, and we have made a simple power-law fit to the effective radiative recombination rate. These estimates are only good to factors of a few. Uncertainty in current knowledge of the UV continuum means that $T_{\rm Balm}$ is uncertain.

The electron density can then be found by solving

$$n_e = n_{\rm H}\left[3.8 \times 10^{-4} + \left(1 + \frac{n_1}{n_2}\frac{n_2}{n_\kappa}\right)^{-1}\right]. \tag{29}$$

Note than when Lyα is not thermalized, the second term on the right-hand side of equation (29) is independent of n_e (HA84). The column densities in our model are significantly higher than in Model 1 of HA84, and the values of n_e implied by the C II UV0.01 λ2325 multiplet suggest that Lyα is thermalized near the T_e-peak of the SEM.

First consider the electron density derived from the C II] 2325 Å diagnostic. At the radius corresponding to the hydrogen column density required for consistent n_e, $R = 1.45\ R_*$ and $n_{\rm H} = 10^{10}$ cm^{-3}. To obtain an ionization fraction of $n_{\rm H\,II}/n_{\rm H\,I} = 0.02$ under these conditions requires $T_e \sim$ 9800 . Again if we assume that the ambient gas component is at 2000 K then this chromospheric temperature is consistent with a filling factor AF $< \frac{1}{4}$. Chromospheric material at this temperature could be an integral part of the mean SEM.

8.4.1. *Extended* Hα *emission*

One of the puzzles posed by the current atmospheric model is where the opacity to scatter Hα off-limb arises. Several Hα observations have been made (Hebden et al. 1986, 1987; Christou et al. 1988) that show Hα is scattered in an extended region above the photosphere of α Ori. Extended Hα scattering has also been observed during the occultation of 119 Tauri (M2 Ib) (White, Kreidel, & Goldberg 1982) and therefore appears to be an intrinsic property of M supergiants. The Hα flux is thought to be mostly scattered photospheric radiation, and therefore the extended atmosphere must have some opacity to this line. The disk integrated Hα profile shows a blue shifted absorption feature that is also consistent with significant opacity present in the extended outflowing region. The H $n = 2$ population is expected to be very small in our mean model when compared to that expected at the chromospheric temperatures ($\sim$8000 K) suggested by previous models. If a component of gas in our mean model were much warmer, however, the wind opacity would increase rapidly and one might expect the warm gas to be detectable in the radio observations. If such gas were dominant, the atmosphere would appear more extended or the gas density would need to be lowered. In either case the combination of size and T_e would be in disagreement with the visibility data.

If the hot component is pervasive enough to scatter the Hα, then why does it not show up in the radio data? Using the simple analytical description described above, we can estimate what temperature inhomogeneities would lead to a significant H $n = 2$ population. We can then determine whether the implied ionization would lead to a dominance in the radio spectrum. For this discussion we assume that there are two components: a background model, which is similar to our mean model, and a hotter component with a small volume filling fraction $F^{\rm vol}$. We assume that the linear filling fraction is $F^{\rm lin} = (F^{\rm vol})^{1/3}$.

The Hα off-limb intensity in α Ori (at say $\phi \sim 40$ mas) does not follow that expected in an optically thin sphere with a constant H $n = 2/n = 1$ ratio, and suggests that either the tangential optical depths are greater than unity or the mean H $n = 2/n = 1$ ratio increases with radius. If we now consider a typical point in the model, say 3 R_*, where the radial hydrogen column density $N_{\rm H} \simeq 9 \times 10^{22}$ cm^{-2} and $W(3R_*) = 0.029$. In the background component our mean model gives $n_e = 3.8 \times 10^{-4} n_{\rm H}$ and $n_{\rm H} = 8 \times 10^8$ cm^{-3}. If we increase the temperature of the hot component, then at $T_e \simeq 5000$ K the Hα opacity becomes equal to the 6.0 cm radio opacity. Above this temperature the Hα opacity exceeds the radio, and plasma that is optically thick in Hα may remain optically thin at 6.0 cm, depending on T_e and $\tau_{\rm H\alpha}$.

Figure 12 (*top*) shows the ratio of 6 cm radio opacity to that of Hα as a function of T_e. The efficiency of gas to scatter Hα increases extremely rapidly with temperature until the $n = 2$ level becomes thermalized as the collisional deexcitation terms becomes important. Both sources of opacity scale with n_e if $n = 2$ is not thermalized. Figure 12 (*bottom*) shows the line center optical depth in Hα, assuming a linear filling factor of unity and that the optical depth is dominated by the contribution from the local density scale height. If $\tau_{\rm H\alpha} > 1$, then $T_e > 5000$ K; however, if the temperature is as high as 8000 K a small linear filling factor is required to avoid strongly enhancing the radio optical depth,

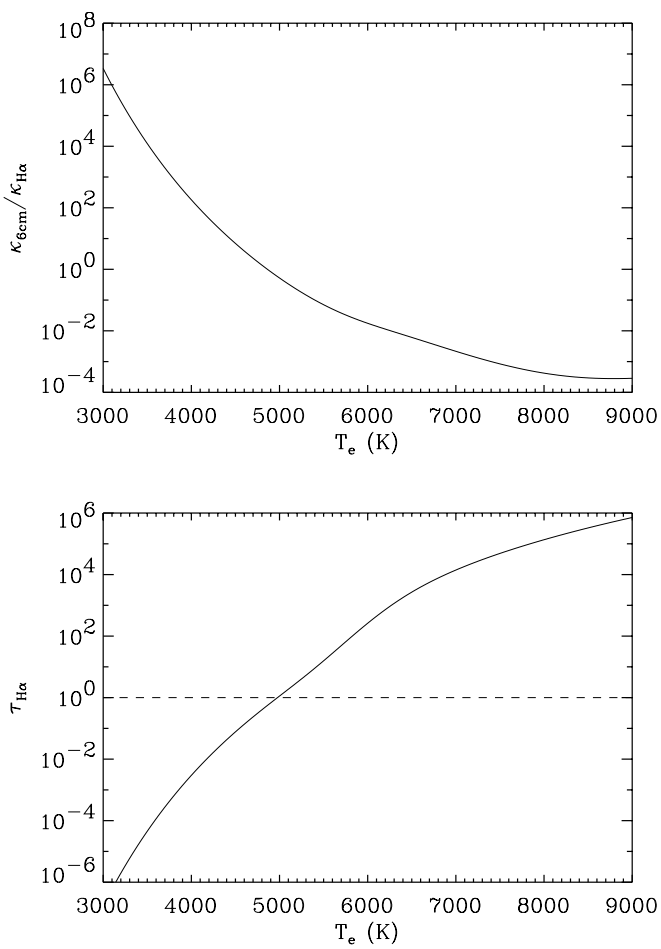

FIG. 12.—Schematic calculation of hydrogen excitation and ionization, and the optical depths of Hα and 6 cm at 3 R_*. *Top:* Ratio of 6 cm radio opacity to Hα as a function of T_e. The Hα opacity rises rapidly with increasing T_e. *Bottom:* Line center optical depth in Hα assuming $f^{\rm lin} = 1$. It can be seen that only a small linear filling factor of material with $T_e \sim 8000$ K is required to satisfy a radial optical depth of unity.

The conditions that most likely to give rise to Hα off-limb scattering and are not be detectable in the multiwavelength visibility radio data are volumes of high-temperature plasma with very small filling factor and $T_e \sim 8000$ K immersed in a cooler mean flow. The column of 8000 K plasma needed to produce a radial optical depth of unity in Hα would be optically thin at 6 cm. In these structures hydrogen ionization will dominate the contribution from photoionized metals.

Given the uncertainties in these estimates and the restricted parameter space for consistent radio and Hα observations, we defer a more detailed comparison to future work. To investigate the radio signature of discrete radial ionized shells, we superposed radial zones of high ionization upon the one-dimensional model and solved for the visibilities. The visibility curves of the continuous model, which are characteristically smooth, develop structure which could be detected with higher signal-to-noise observations. If such structures do occur, the ongoing VLA upgrade should allow these structures to be detected and perhaps allow the evolution of these structures to be followed.

New off-limb high S/N observations of Hα with precise spectral characterization of the filters may provide the vital clues needed to understanding the geometry of the hot plasma and hence elucidate the, as yet unknown, mechanisms that heat the atmosphere and winds of evolved late-type stars.

9. CONCLUSIONS

Below we summarize the main conclusions from the modeling of the VLA visibility data of α Ori.

1. Photoionized metals (mostly C) are the dominant source of free electrons in the radio-emitting region.
2. H^-(free-free) opacity dominates in the radio, but free-free opacity from weakly ionized hydrogen at warmer temperatures and free-free opacity from photoionized metals at lower temperatures still contribute.
3. The radio opacity is a weak function of T_e, since n_e is from photoionized metals, which enables a simple modeling of the radial density distribution.
4. The peak in the temperature distribution at $R = 1.45$ R_* appears to be consistent, in density and column density with the C II UV0.01 chromospheric emitting region if the filling factor $\leq \frac{1}{4}$ with $T_{\rm chrom} \sim 9800$ K.
5. Warm material ($T_e \sim 8000$ K) with a very small filling factor is the simplest way to reconcile the cool extended mean model with the observed off-limb Hα scattering.
6. The wind absorption features observed in the UV Fe II emission lines suggest that the density model based on the radio visibilities may be part of the overall mass outflow, with a mass-loss rate of $3.1 \pm 1.3 \times 10^{-6}$ $M_\odot$ yr^{-1}. This value is consistent with independent circumstellar estimates.
7. A simple silicate dust model with a dust-to-gas mass ratio of $f_D = 5.8 \times 10^{-4}$ appears to reproduce the salient observations. The dust appears to form near 33 R_* (i.e., 0″.9 from star center).
8. Further progress requires high S/N visibility data at the longer VLA baselines, and interferometry at wave-

lengths less than 0.7 cm. This would enable the poorly understood region between the temperature peak and photosphere to be better constrained.

It is very important to establish whether the outward decrease in T_e starting close to the star, near $R = 1.45\ R_*$, is a general property of winds from evolved stars with earlier and less evolved spectral types. The only reliable way to do this with radio data is to resolve stars at two or more frequencies. Work is urgently needed to refine the stellar parameters of α Ori, to understand the nature of its variability, and the differences in angular diameters measured at different wavelengths.

G. M. H. thanks E. Avrett for providing detailed information from the 1984 Alfvén wave models and (posthumously) C. Skinner for making his VLA/MERLIN radio visibility data available prior to publication. Thanks also to Irene and Steve Little for discussions on silicate dust models, Philip Bennett for suggesting the analytical density model, Jeffrey Linsky for suggesting material for inclusion, and to the numerous colleagues who helped stimulate this research. We would also like to thank K. G. Carpenter, J. J. Sudol, A. Lançon, and K. Justtanont for their assistance in providing data in computer readable format. This research has made extensive use of NASA's Astrophysics Data System Abstract Service. G. M. H.'s research was funded from NASA grant NAG 5-4808, and A. B.'s contribution from NASA grant NAG 5-3226.

APPENDIX A

IDEALIZED ANALYTICAL MODEL FOR BENCHMARKING THE NUMERICAL RADIATIVE TRANSFER CODES

In this section we briefly outline a simple analytical model for the centimer-radio fluxes in which the thermodynamic properties are described as power laws in the radial distance; in particular; we allow for a radially varying source function, i.e., T_e. The use of power laws allows some analytical development—see Schmid-Burgk (1982) and Seaquist & Taylor (1987) for work including a variable source function. Seaquist & Taylor use the power-law approximations to directly fit the visibilities of RX Puppis. We derive simple approximations for the wind radio emission when it is dominated by H^-(free-free). We use the previously known closed solution for this problem (Schmid-Burgk 1982) to benchmark the accuracy of the model fluxes under reasonable physical conditions.

At centimeter wavelengths the source function (S_ν) is essentially given by the Planck function in the Rayleigh-Jeans approximation, i.e.,

$$S_\nu \simeq \frac{2\nu^2 k T_e}{c^2}\,, \tag{A1}$$

where ν is the frequency and k is the Boltzmann constant. We make a power-law approximation for the wind opacity

$$\kappa_\nu = \text{const} \times \nu^f T_e^t Z_{\text{ion}}^2 n_e n_i\,, \tag{A2}$$

where n_i is the number of ions or neutrals with which the electrons interact. For H^- opacity we set $Z_{\text{ion}} = 1$. The expression for the H^- free-free opacity is from Mezger & Henderson (1967) and based on an approximation by Altenhoff et al. (1960). The coefficients for H^-, H^-free-free, and a mixture corresponding to $n_e/n_{\text{H}} = 3.8 \times 10^{-4}$ are given in Table 8.

In the following we shall consider the case where the atmospheric properties can be represented by power laws. We write the ion and electron density as functions of the hydrogen nuclei density [$n(\text{H}) = n_{\text{H I}} + n_{\text{H II}}$], i.e.,

$$n_{\text{imp}} = f_{\text{imp}} n_{\text{H}} \quad \text{and} \quad n_{\text{ele}} = f_{\text{ele}} n_{\text{H}}\,, \tag{A3}$$

and, further, each of these terms in the opacity is expressed as a power law:

$$n_{\text{H}}(R) = n_{\text{H},o}(R_o)\left(\frac{R_o}{R}\right)^q\,, \tag{A4}$$

$$f_{\text{imp}}(R) = f_{\text{imp},o}(R_o)\left(\frac{R_o}{R}\right)^a\,, \tag{A5}$$

$$f_{\text{ele}}(R) = f_{\text{ele},o}(R_o)\left(\frac{R_o}{R}\right)^b\,, \tag{A6}$$

TABLE 8

ABSORPTION COEFFICIENT DEPENDENCIES: ν IN HZ AND T_e IN K.

	H Free-Free	H^- Free-Free	Mixture ($n_e/n_{\text{H}} = 3.8 \times 10^{-4}$)
Const.....	0.2120	6.20×10^{-11}	6.50×10^{-9}
f.....	−2.1	−2.0	−2.0
t.....	−1.35	+0.22	−0.30
n_i	n_{ion}	$n_{\text{H I}}$	$n_{\text{H I}}$
Z_{ion}	Z_{ion}	1.0	1.0

$$Z_{\rm ion}(R) = Z_{{\rm ion},o}(R_o)\left(\frac{R_o}{R}\right)^c , \tag{A7}$$

$$T_e(R) = T_{e,o}(R_o)\left(\frac{R_o}{R}\right)^d . \tag{A8}$$

Here $q > \frac{1}{2}$. When $q = 2$ the density is the same as for the constant velocity wind case. In spherical geometry, note that when $q \leq 3$ the mass of the system is formally unbound; however, by choosing an arbitrary outer radius, e.g., ISM interface, finite physical size, or lifetime, this does not present a problem as we are considering a finite region near the star. The Rayleigh-Jeans source function is then written as

$$S_\nu(T_e) = \frac{2\nu^2 k T_{e,o}}{c^2}\left(\frac{R_o}{R}\right)^d . \tag{A9}$$

Analytical integration for the specific intensity and then over angle in the sky can be shown to give the observed flux

$$F_\nu = 2\pi\left(\frac{\phi_*}{2}\right)^2 \frac{2\nu^2 k T_{e,o}}{c^2}\left(\frac{R_o}{R_*}\right)^d \sigma_\nu^{2-d} \times \mathscr{F}(d, \Pi) , \tag{A10}$$

where $\mathscr{F}(d, \Pi)$ is a geometrical function that is independent of frequency and can be evaluated once for each combination of d and Π. The angular diameter ϕ_* corresponds to the radial distance R_*.$\mathscr{F}(d, \Pi)$ is given by

$$\mathscr{F}(d, \Pi) = \int_{s=0}^{\infty}\int_{l=-\infty}^{+\infty} \frac{s}{(l^2 + s^2)^{d/2+\Pi/2}} \exp\left\{-\int_{-\infty}^{l} \frac{1}{(l^2 + s^2)^{\Pi/2}} dl\right\} ds\, dl , \tag{A11}$$

where

$$\Pi = 2q + a + b + 2c + t \times d \tag{A12}$$

and d is the power-law exponent for T_e. The frequency dependent scaling term σ_ν is given by

$$\sigma_\nu = \left({\rm const} \times \nu^f T_{e,o}^t\, f_{{\rm imp},o}\, f_{{\rm ele},o}\, n_{{\rm H},o}^2\, R_o^\Pi \frac{1}{R_*^{\Pi-1}}\right)^{1/(\Pi-1)} , \tag{A13}$$

where the values of const and f are given in Table 2 for the different cases where H(free-free) or H^-(free-free) opacity dominates.

The spectral index, $S_\nu \propto \nu^\alpha$ is then given by

$$\alpha = \frac{2a + 2b + 4c + 4q - 2 + 2t \times d + 2 \times f - d \times f}{a + b + 2c + 2q + t \times d - 1} . \tag{A14}$$

Given the ϕ_*, the values of the thermodynamic quantities at R_o and the power-law indices (q, a, b, c, d) the flux and spectral index can be found. To test our numerical codes we adopt the test case characterized in Table 9.

We adopt the radio opacity for the *mixture* of opacities representative of the atmosphere outside the peak in the T_e distribution.

The spectral index for this model is $\alpha = 1.44$. The flux at 3.54 cm is 3.490 mJy with $\mathscr{F}(d = 0.740, \Pi = 5.478) = 0.795$. The one-dimensional radiative transfer code with 200 shells gives a flux of 3.492 mJy indicating a computational error from the discretization in the formal solution and in the angle quadratures of less than 1%. For the very extended dust computations, which extend to 5′, the depth grid (500 points) will lead to a somewhat degraded accuracy.

The model flux slightly exceeds that observed since the power-law model for T_e breaks down for $R < 1.8\ R_*$, with the temperature being less than the power-law model. The opacity at 3.54 cm is insufficient to shield the material below, so the analytical value is an overestimate. For 6.17 and 20.5 cm the power-law model gives 1.57 and 0.28 mJy.

TABLE 9

ADOPTED BENCHMARK PARAMETERS

Value at R_o	Power-Law Index
$f_{{\rm imp},o} = 1.0$	$a = 0.00$
$f_{{\rm ele},o} = 3.8 \times 10^{-4}$	$b = 0.00$
$z_{{\rm ion},o} = 1.0$	$c = 0.00$
$T_{e,o} = 3720.0$	$d = 0.74$
$n_{{\rm H},o} = 3.5 + 10^9$	$q = 2.85$

NOTE.—Reference radial scale: $\phi = 56.0$ mas, $R_* = 789\ R_\odot$, and $R_o = 1.8\ R_*$.

APPENDIX B

H^- FREE-FREE OPACITY FOR $10 < T_e(\mathrm{K}) \leq 1400$

Published values for H^- free-free opacity have focused on warmer temperatures than those encountered in the extended atmosphere of α Ori (Lim et al. 1998) and Mira and semiregular variable stars (Reid & Menten 1997). The best available opacities of Bell & Berrington (1987, hereafter BB87) are tabulated down to $T_e = 1400$ K, with the longest wavelength being 15.1 μm. John (1988) has made polynomial fits to these data and extrapolated the wavelength range to $\lambda \to \infty$.

Here we give approximate values for the H^- opacity for the lower temperatures necessary to study α Ori. The opacities are based on interpolations of phase-shifts for elastic scattering of electrons by neutral hydrogen, combined with the low photon energy approximation for the matrix elements of the dipole radiation formula. These matrix elements from John (1994, eq. [6]) are exact in the low photon energy limit. The form of the phase-shift interpolations are based on the modified effective range theory (O'Malley, Spruch, & Rosenberg 1961; O'Malley, Rosenberg, & Spruch 1962). These authors give expansions for the phase shifts in terms of the free electron momentum (k_0) and whose coefficients are given in terms of scattering lengths, atomic polarization and fits to detailed computations for different k_0. The opacities given here are computed in the spirit of Dalgarno & Lane (1966), who also used the modified effective range theory.

Here we wish to bridge the gap between the results of BB87 and the low temperature, low photon energy limit. An upper bound for the opacity in the low photon energy limit was obtained by John (1966) but is of little practical value in the present circumstance. The aim here being to quantifying the uncertainty in the resulting opacities in the regime $10 < \lambda(\mu\mathrm{m}) < \infty$ and $10 < T_e(\mathrm{K}) < 2520$. The important parameter $h\nu/kT_e$ covers a wide range of values, and the stimulated emission term $(1 - \exp\{-h\nu/kT_e\})$ is used explicitly. The adopted phase shifts for singlet and triplet scattering are the following: S-wave (Shimamura 1971); zero-energy S-wave (Schwartz, 1961); P and D-wave (BB87, Table 4). There is good agreement between the phase shifts of BB87 and other variational calculations (e.g., Armstead 1968). Higher total orbital angular momentum states were included using the expression of O'Malley et al. (1961, eq. [5.9]). The polarization for hydrogen is $4.5a_0^3$, where a_0 is the Bohr radius. Figure 13 shows the opacity computed using the approximations described above for $\lambda = 9.1134$ μm (*solid curve*). The empty circles show the detailed *R*-matrix calculations of BB87. In the region of overlap between the present computations and those of BB87 the agreement is within 2%. The range of validity of our approximation is restricted to $10 < \lambda(\mu\mathrm{m}) < \infty$ and $3 < T_e(\mathrm{K}) < 2520$.

The dashed curve in Figure 13 shows a simpler approximation which should be useful for rough calculations. We base this approximation on a single point evaluation of the low-T_e, long-wavelength limit for the expression for H^- opacity (Chandrasekhar & Breen 1946). In this approximation the opacity (cm^{-1}) is given per neutral hydrogen atom per electron for λ in cm, and T_e in Kelvin.

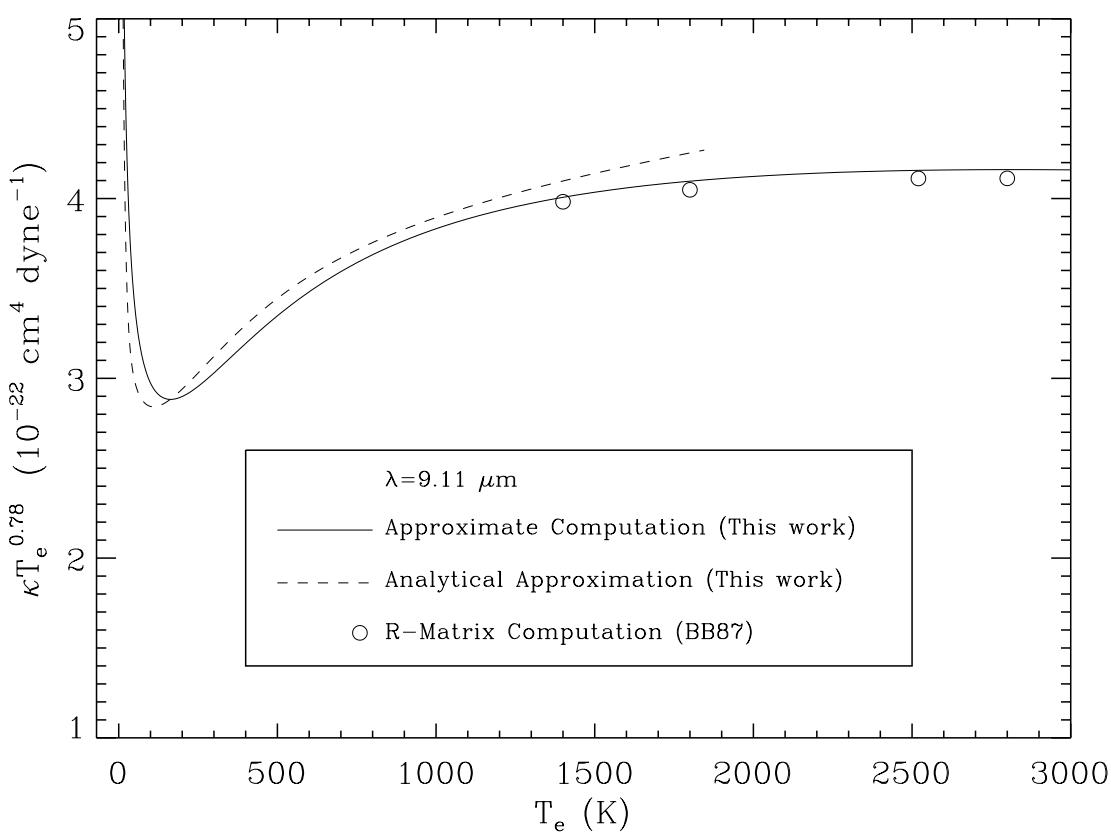

FIG. 13.—H^- (free-free) radio opacity for low temperatures, and low photon energies. The opacity is plotted multiplied by $T_e^{0.78}$(K) to show the T_e dependence near 1500 K. Note that here the opacity is given in units of cm^4 dyne^{-1}.

$$\kappa(\lambda, T_e) = 6.82 \times 10^{-33}\lambda^3 T_e^{3/2}(1 - \exp\{-\beta\})(1 + \alpha\beta/2)(1 + \alpha\beta)^{1/2} f(T_e) , \quad \text{(B1)}$$

where $\beta = 1.439/(T_e \lambda)$, α corresponds to an evaluation energy, and $f(T_e)$ is a function to detrend the differences between the approximate and computed opacities. Neglecting this correction, i.e., $f(T_e) \equiv 1$ then with $\alpha = 0.83$ the approximation is better than 50% for the entire range. However, if we set $\alpha = 0.66$ and

$$f(T_e) = (1 - 0.28 \exp\{-800/T_e\})(1 + 2.5 \exp\{-150\lambda T_e\}) , \quad \text{(B2)}$$

the approximation is good to better than 20% for the range. For $\lambda > 1$ cm the fit is good to 11%.

In this paper we use the results of BB87 as fit by John (1988) for $T_e > 1400$ K and for values below this we use the later approximate expression. Since the completion of this work John has kindly provided us with opacities for long wavelengths and low temperatures calculated with accurate wave function data. His values are about 1%–5% lower than our values which we used to derive the simple approximations above.

REFERENCES

Altenhoff, W. J., Mezger, P. G., Wendker, H., & Westerhout, G. 1960, Veröff. Sternwärte, Bonn, No. 59, 48
Altenhoff, W. J., Thum, C., & Wendker, H. J. 1994, A&A, 281, 161
Armstead, R. L. 1968, Phys. Rev., 171, 91
Avrett, E. H., & Loeser, R. 1992, in ASP Conf. Ser. 26, Cool Stars, Stellar Systems, and the Sun, eds. M. S. Giampapa & J. A. Bookbinder (San Francisco: ASP), 26, 489
Barlow, M. J. 1999, IAU Symp. 191, Asymptotic Giant Branch Stars, ed. A. Lebre, T., le Berte, & C. Waelkens (San Francisco: ASP), 353
Baschek, B., Scholz, M., & Wehrse, R. 1991, A&A, 246, 374
Basri, G. S., Linsky, J. L., & Eriksson, K. 1981, ApJ, 251, 162
Bell, K. L., & Berrington, K. A. 1987, J. Phys. B., 20, 801
Bennett, P. D. 1991, Ph.D. Thesis, Univ. British Columbia
Bernat, A. P. 1977, ApJ, 213, 756
Bernat, A. P., Hall, D. N. B., Hinkle, K. H., & Ridgway, S. T. 1979, ApJ, 233, L135
Bernat, A. P., & Lambert, D. 1975, ApJ, 201, L153
———. 1976, ApJ, 210, 395
Bessell, M. S. 1990, PASP, 102, 1181
Bessell, M. S., & Brett, J. M. 1988, PASP, 106, 1134
Bessell, M. S., Castelli, F., & Plez, B. 1998, A&A, 333, 231
Bester, M., Danchi, W. C., Hale, D., Townes, C. H., Degiacomi, C. G., Mékarnia, & Geballe, T. R. 1996, ApJ, 463, 336
Black, J. H. 1987, in Spectroscopy of Astrophysical Plasmas, ed. A. Dalgarno & D. Layzer (New York: Cambridge Univ. Press), 279
Blackwell, D., E., & Shallis, M. J. 1977, MNRAS, 188, 847
Boesgaard, A. M. 1979, ApJ, 232, 485
Boesgaard, A. M., & Magnan, C. 1975, ApJ, 198, 369
Bowers, P. F., & Knapp, G. R. 1987, ApJ, 315, 305
Brown, J. A., Johnson, H. R., Alexander, D. R., Cutright, L. C., & Sharp, C. M. 1989, ApJS, 71, 623
Burns, D., et al. 1997, MNRAS, 290, L11
Cardelli, J. A., Clayton, G. C., & Mathis, J. S. 1989, ApJ, 345, 245
Carlsson, M., & Stein, R. F. 1995, ApJ, 444, L29
Carpenter, K. G. 1984, ApJ, 285, 181
Carpenter, K. G., Norman, D., Robinson, R. D., Fernandez-Villacanas, J. L., Jordan, C., & Judge, P. G. 1990, in Evolution in Astrophysics: *IUE* Astronomy in the Era of New Space Missions, ed. E. J. Rolfe (ESA SP310; Paris: ESA), 307
Carpenter, K. G., & Robinson, R. D. 1997, ApJ, 479, 970
Carpenter, K. G., Robinson, R. D., & Judge P. G. 1995, ApJ, 444, 424
Carpenter, K. G., Robinson, R. D., Harper, G. M., Bennett, P. D., & Brown, A. 1999, ApJ, 428, 329
Carpenter, K. G., Robinson, R. D., Judge, P. G., Ebbets, D. C., Brandt, J. C. 1994, in ASP Conf. Ser. 64, Cool Stars, Stellar Systems, and the Sun, ed. J.-P. Caillault (San Francisco: ASP), 56
Carpenter, K. G., & Robinson, R. D., Wahlgren, G. M., Linsky, J. L., & Brown, A. 1994b, ApJ, 428, 329
Cassinelli, J. P., & Hartmann, L. 1977, ApJ, 212, 488
Chandrasekhar, S., & Breen, F. H. 1946, ApJ, 104, 430
Cheng, A. Y. S., Hege, E. K., Hubbard, E. N., Goldberg, L., Strittmatter, P. A., & Cocke, W. J. 1986, ApJ, 309, 737
Christou, J. C., Hebden, J. C., & Hege, E. K. 1988, ApJ, 327, 894
Dalgarno, A., & Lane, N., F. 1966, ApJ, 145, 623
Danchi, W. C., Bester, M., Degiacomi, C. G., Greenhill, L. J., & Townes, C. H. 1994, AJ, 107, 1469
David, P., & Pégourié, B. 1995, A&A, 293, 833
Drake, S. A., Bookbinder, J. A., Florkowski, D. R., Linksy, J. L., Simon, T., & Stencel, R. E. 1992, in ASP Conf. Ser. Vol. 26, Cool Stars, Stellar Systems, and the Sun, ed. M. S. Giampapa & J. A. Bookbinder (San Francisco: ASP), 455
Drake, S. A., & Linsky, J. L. 1986, AJ, 91, 602
Drake, S. A., Linsky, J. L., & Elitzur, M. 1987, AJ, 94, 1280
Dupree, A. K., Baliunas, S. L., Guinan, E. F., Hartmann, L., Nassiopoulos, G. E., & Sonneborn, G. 1987, ApJ, 317, L85
Dupree, A. K., & Reimers, D. 1987, in Exploring the Universe with the *IUE* Satellite, ed. Y. Kondo (Dordrect: Kluwer), 321
Dyck, H. M., Benson, J. A., Ridgway, S. T., & Dixon, D. J. 1992, AJ, 104, 1982
Dyck, H. M., Benson, J. A., van Belle, G. T., & Ridgway, S. T. 1996, AJ, 111, 1705
Engelke, C. W. 1992, AJ, 104, 124
ESA. 1997, The Hipparcos and Tycho Catalogues (ESA SP-1200; Noordwijk: ESA)
Fensl, R. M. 1995, A&AS, 112, 191
Fomalont, E. B., & Wright, M. C. H. 1974, in Galactic and Extragalactic Radio Astronomy, ed. G. L. Vershuur & K. I. Kellerman (New York: Springer), 256
Fruscione, A., Hawkins, I., Jelinsky, P., & Wiercigroch, A. 1994, ApJS, 94, 127
Gilliland, R., & Dupree, A. K. 1996, ApJ, 436, L29
Glassgold, A. E., & Huggins, P. J. 1986, ApJ, 306, 605
Goldberg, L. 1979, QJRAS, 20, 361
———. 1984, PASP, 96, 368
Guilain, C., & Mauron, N. 1996, A&A, 314, 585
Hartmann, L., & Avrett E. H. 1984, ApJ, 284, 238 (HA84)
Haas, M. R., & Glassgold, A. E. 1993, ApJ, 410, L111
Harper, G. M. 1994, MNRAS, 268, 894
Harper, G. M., Wood, B. E., Linsky, J. L., Bennett, P. D., Ayres, T. R., & Brown, A. 1995, ApJ, 452, 407
Hebden, J. C., Christou, J. C., Cheng, A. Y. S., Hege, E. K., Strittmatter, P. A., Beckers, J. M., & Murphy, H. P. 1986, ApJ, 309, 745
Hebden, J. C., Eckart, A., & Hege, E. K. 1987, ApJ, 314, 690
Hinz, P. M., Angel, J. R. P., Hoffmann, W. F., McCarthy, D. W., Jr., McGuire, P. C., Cheselka, M., Hora, J. L., & Woolf, N. J. 1998, Nature, 395, 251
Hjellming, R. M., & Newell, R. T. 1983, ApJ, 275, 704
Hofmann, K.-H., & Scholz, M. 1998, A&A, 335, 637
Holzer, T. E., & MacGregor, K. B. 1985, in Mass-Loss from Red Giants, ed. M. Morris & B. Zuckermann (Dordrecht: Reidel), 229
Honeycutt, R. K., Bernat, A. P., Kephart, J. E., Gow, C. E., Sandford, II, M. T., & Lambert, D. L. 1980, ApJ, 239, 565
Huggins, P. J. 1987, ApJ, 313, 400
Huggins, P. J., Bachiller, Cox, P., & Forveille, T. 1994, ApJ, 424, L127
Hummer, D. G. 1988, ApJ, 327, 477
Jewell, P. R., Snyder, L. E., Walmsley, C. M., WIlson, T. L., Gensheimer, P. D. 1991, A&A, 242, 211
John, T. L. 1966, MNRAS, 131, 315
———. 1975, MNRAS, 170, 5
———. 1988, A&A, 193, 189
———. 1994, A&A, 282, 890
Judge, P. G., & Carpenter, K. G. 1998, ApJ, 494, 828
Jura, M. 1996, ApJ, 472, 806
Justtanont, K., Tielens, A. G. G. M., de Jong, T., Wateres, L. B. F. M., & Yamamura, I. 1999, A&A, 345, 605
Keenan, P. C., & McNeil, R. C. 1989, ApJS, 71, 245
Kiehling, R. 1987, A&AS, 69, 465
Klückers, V. A., Edmunds, M. G., Morris, R. H., & Wooder, N. 1997, MNRAS, 284, 711
Knapp, G. R. 1985, ApJ, 293, 273
Knapp, G. R., & Bowers, P. F. 1988, ApJ, 331, 974
Knapp, G., R., Phillips, T. G., & Huggins, P. J. 1980, ApJ, 242, L25
Kunasz, P. B., & Auer, L. H. 1988, J. Quant. Spcectrosc. Radiat. Trans., 39, 67
Lambert, D. L., Brown, J. A., Hinkle, K. H., & Johnson, H. R. 1984, ApJ, 284, 223
Lambert, D. L., & Snell, R. L. 1975, MNRAS, 172, 277
Lambert, D. L., & van den Bout, P. A., 1978, ApJ, 221, 854
Lançon, A., & Rocca-Volmeragne, B. 1992, A&AS, 96, 593
Landini, M., & Monsignori Fossi, B. C. 1990, A&AS, 82, 229
Le Borgne, J. F., Mauron, N., & Leroy, J. L.1986, A&A, 168, 211
Lim, J., Carilli, C. L., White, S. M., Beasley, A. J., & Marson, R. G. 1998, Nature, 392, 575
Lorenz-Martins, S., Lefèvre, J., & Mékarnia, D. 1995, A&A, 300, 214

Marshall, C. R., Leahy, D. A., & Kwok, S. 1992, PASP, 104, 397
Mathisen, R. 1984, Inst. Theor. Astrophys, Univ Oslo, Pub. Ser. No. 1
Mauron, N. 1990, A&A, 227, 141
Mauron, N., & Caux, E. 1992, A&A, 265, 711
Mauron, N., & Le Borgne, J. F. 1986, A&A, 168, 217
McMillan, R. S., & Tapia, S. 1978, ApJ, 226, L87
Mezger, P. G., & Henderson, A. P. 1967, ApJ, 147, 471
Morgan, N., D., Wasatonic, R., & Guinan, E. F. 1997, Int. Bull. Variable Stars, 4499
Newell, R. T., & Hjellming, R. M. 1982, ApJ, 263, L85
Noriega-Crespo, A., Van Buren, D., Cao, Y., & Dgani, R. 1997, AJ, 114, 837
Olnon, F. M. 1975, A&A, 39, 217
Olson, G. L., & Kunasz, P. B. 1987, J. Quant. Spcectrosc. Radiat. Trans., 38, 325
O'Malley, T. F., Rosenberg, L., & Spruch, L. 1962, Phys. Rev., 125, 1300
O'Malley, T. F., Spruch, L, & Rosenberg, L. 1961, J. Math. Phys., 2, 491
Panagia, N., & Felli, M. 1975, A&A, 39, 1
Paresce, F. 1984, AJ, 89, 1022
Reid, M. J., & Menten, K. M. 1997, ApJ, 476, 327
Rinehart, S. A., Hayward, T. L., & Houck, J. R. 1998, ApJ, 503, 415
Rodgers, B., & Glassgold, A. E. 1991, ApJ, 382, 606
Rowan-Robinson, M., & Harris, S. 1982, MNRAS, 200, 197
Rowan-Robinson, M., Lock, T. D., Walker, D. W., & Harris, S. 1986, MNRAS, 222, 273
Rybicki, G. B. 1984, in Methods in Radiative Transfer, ed. W. Kalkofen (Cambridge: Cambridge Univ. Press), 21
Ryde, N., Gustafsson, B., Hinkle, K., Eriksson, K., Lambert, D. L., & Olofsson, H. 1999, A&A, 347, L35
Sanner, F. 1976, ApJS, 32, 115
Scheuer, P. A. G. 1960, MNRAS, 120, 231
Schmid-Burgk, J. 1982, A&A, 108, 169
Scholz, M., & Takeda, Y. 1987, A&A, 186, 200
Scholz, T. T., & Walters, H. R. J. 1991, ApJ, 380, 302
Schröder, K. -P., Griffin, R. E. M., & Griffin, R. F. 1990, A&A, 234, 299
Schwartz, C. 1961, Phys. Rev., 124, 1468
Seab, C. G., & Snow, T. P. 1989, ApJ, 347, 479
Seaquist, E. A., & Taylor, A. R. 1987, ApJ, 312, 813
I. 1971, J. Phys. Soc. Japan, 30, 1702
Shull, J. M., & van Steenberg, M. 1982, ApJS, 48, 95
Schutte, W. A., & Tielens, A. G. G. M. 1989, ApJ, 343, 369
Skinner, C. J., Dougherty, S. M., Bode, M. F., Drake S. A., & Davis, R. J. 1996, in ASP. Conf. Ser. 93, Radio Emission from the Stars and Sun (San Francisco: ASP), 113
Skinner, C. J., Dougherty, S. M., Meixner, M., Bode, M. F., Davis, R. J., Drake, S. A., Arens, J. F., & Jernigan, J. G. 1997, MNRAS, 288, 295
Skinner, C. J., & Whitmore, B. 1987, MNRAS, 224, 335
Smith, M. A., Patten, B. M., & Goldberg, L. 1989, AJ, 98, 2233
Sopka, R. J., Hildebrand, R., Jaffe, D. T., Gatley, I., Roellig, T., Werner, M., Jura, M., & Zuckermann, B. 1985, ApJ, 294, 242
Stencel, R. E., Pesce, J. E., & Hagen Bauer, W. 1988, AJ, 95, 141
Straižys, V. 1992, Multicolor Stellar Photometry (Tuscon: Pachart)
Sudol, J. J. 2000 Ph.D. thesis, Univ. Wyoming
Sudol, J. J., Dyck, H. M., Stenvel, R. E., Klebe, D. I., & Creech-Eakman, M. J. 1999, ApJ, 117, 1609
Tondello, G. 1972, ApJ, 172, 771
Tsuji, T. 1978, PASJ, 30, 435
Tsuji, T., Ohnaka, K., Hinkle, K. H., & Ridgway, S. T. 1994, A&A, 289, 469
Tuthill, P. G., Haniff, C. A., & Baldwin, J. E. 1997, MNRAS, 285, 529
Uitenbroek, H., Dupree, A. K., & Gilliland, R. L. 1998, AJ, 116, 2501
van de Hulst, H. C. 1981, Light-Scattering by Small Particles (: New York: Dover)
van der Veen, W. E. C. J., Huggins, P. J., Matthews, H. E. 1998, ApJ, 505, 749
Vieira, T. 1986, Uppsala Astron. Obs, Rep. 32, The Chemicl Composition of Two Late-Type Stars: alpha Orionis and HD 115444 (Uppsala: Uppsala Astron. Obs.)
Walder, R., & Harper, G. M. 1996, in ASP Conf. Ser. 109, Cool Stars, Stellar Systems, and the Sun, ed. R. Pallavicini & A. K. Dupree (San Francisco: ASP), 553
Weymann, R. 1962, ApJ, 136, 844
White, N. M. 1980, ApJ, 242, 646
White, R. L., & Becker, R. H. 1982, ApJ, 262, 657
White, N. M., Kreidel, T. J., & Goldberg, L. 1982, ApJ, 254, 670
Wilson, R. W., Dhillon, V. S., & Haniff, C. A. 1997, MNRAS, 291, 819
Wickramasinghe, N. C. 1973, Light Scattering Functions for Small Particles, with Applications in Astronomy (London: Adam Hilger).
Wischnewski, E., & Wendker, H. J. 1981, A&A, 96, 102
Wright, A. E., & Barlow, M. J. 1975, MNRAS, 170, 41